



HAL
open science

Design of Reactive Particle Fluidized Bed Heat Exchangers for Gas–Solid Thermochemical Energy Storage

Hangbin Zheng, Xianglei Liu, Gilles Flamant

► **To cite this version:**

Hangbin Zheng, Xianglei Liu, Gilles Flamant. Design of Reactive Particle Fluidized Bed Heat Exchangers for Gas–Solid Thermochemical Energy Storage. *Chemical Engineering Journal*, 2024, 489, pp.151305. 10.1016/j.cej.2024.151305 . hal-04751096

HAL Id: hal-04751096

<https://cnrs.hal.science/hal-04751096v1>

Submitted on 25 Oct 2024

HAL is a multi-disciplinary open access archive for the deposit and dissemination of scientific research documents, whether they are published or not. The documents may come from teaching and research institutions in France or abroad, or from public or private research centers.

L'archive ouverte pluridisciplinaire **HAL**, est destinée au dépôt et à la diffusion de documents scientifiques de niveau recherche, publiés ou non, émanant des établissements d'enseignement et de recherche français ou étrangers, des laboratoires publics ou privés.



Distributed under a Creative Commons Attribution - NonCommercial - NoDerivatives 4.0 International License



Design of reactive particle fluidized bed heat exchangers for gas–solid thermochemical energy storage

Hangbin Zheng^{a,c}, Xianglei Liu^{a,b}, Gilles Flamant^{c,*}

^a School of Energy and Power Engineering, Nanjing University of Aeronautics and Astronautics, Nanjing 210016, China

^b Key Laboratory of Thermal Management and Energy Utilization of Aviation Vehicles, Ministry of Industry, and Information Technology, Nanjing, Jiangsu 210016, China

^c Processes, Materials and Solar Energy Laboratory, PROMES-CNRS, 7 Rue Du Four Solaire 66120 Font Romeu, France

ARTICLE INFO

Keywords:

Calcium looping
Thermochemical energy storage
Fluidized bed
Heat exchanger
Supercritical carbon dioxide cycle

ABSTRACT

Concentrated solar power (CSP) systems integrated with a supercritical carbon dioxide (sCO₂) Brayton power cycle are regarded as the primary future direction for CSP technologies. Calcium-based particles can be a suitable storage medium to achieve high temperatures exceeding 750 °C. However, there have been few studies on reactive particle/sCO₂ heat exchangers (HXs) to drive high-performance power cycles with high energy storage efficiencies. In this paper, the mechanisms by which chemically reactive particles release energy in a fluidized bed (FB) heat exchanger has been investigated to evaluate the performance of thermochemical storage systems. A 1-MW_t thermal duty fluidized bed heat exchanger with sCO₂ as the working fluid operating at 988 K was designed in different configurations, featuring single stage and multistage counter-flow HXs. A detailed shell and tube model combining the chemical reaction kinetics and the heat transfer between the fluidized particle and sCO₂ FB HX design was developed. A comparison of sensible and chemical heat materials shows that thermochemical energy storage is advantageous due to the relatively short tube length and slow particle mass flow rate. The tube length and particle mass flow rate are reduced by 3.5 and 11.5 times, respectively. The average chemical conversion is 97.30 % for a one-stage heat exchanger, which is lower than the 99.95 % conversion achieved by the two-stage heat exchanger. Additionally, a sensitivity analysis was carried out to understand the impacts of key operating parameters on the process performance. These findings provide insights into the operational stability and efficiency of the system, contributing to the development of advanced heat exchangers for thermochemical energy storage applications.

Nomenclature

$A_{\text{tube},i}$	wetted surface area of the heat exchanger (m ²)
$Ar_{g,i}$	Archimedes number (–)
$C_{p,g,i}$	heat capacity of the fluidized gas (J/kg/K)
$C_{p,s\text{CO}_2,i}$	heat capacity of the sCO ₂ (J/kg/K)
$C_{p,s,i}$	heat capacity of the particle (J/kg/K)
C_{p,CaCO_3}	heat capacity of CaCO ₃ (J/kg/K)
$C_{p,\text{CARBO}}$	heat capacity of CARBO particles (J/kg/K)
C	concentration of CO ₂ inside the particle (mol/m ³)
C_e	equilibrium concentration of CO ₂ (mol/m ³)
d_p	particle diameter (m)
$D_{\text{tube,out}}$	external tube diameter (m)
$D_{\text{tube,in}}$	internal tube diameter (m)
D_p	product layer diffusion coefficient (m ² /s)
D_{p0}	product layer diffusion prefactor (m ² /s)

(continued on next column)

Nomenclature (continued)

D_s	surface diffusion coefficient (m/s)
D_{s0}	surface diffusion coefficient prefactor (m/s)
e	thickness of the tube (mm)
$E(t)$	residence time distribution of the particles in a stage (–)
E_k	activation energy of the carbonation reaction (kJ/mol)
E_p	activation energy of product layer diffusion (kJ/mol)
E_s	activation energy of surface diffusion (kJ/mol)
f_i	friction factor of the tube (–)
g	acceleration of gravity (m/s ²)
gD	geometric model function (–)
$h_{s\text{CO}_2,i}$	sCO ₂ side heat transfer coefficient (W/m ² /K)
$h_{p,i}$	particle-side heat transfer coefficient (W/m ² /K)
$h_{p,\text{SingleTube}}$	particle-side heat transfer coefficient for single tube (W/m ² /K)

(continued on next page)

* Corresponding author.

E-mail address: Gilles.Flamant@promes.cnrs.fr (G. Flamant).

<https://doi.org/10.1016/j.cej.2024.151305>

Received 27 October 2023; Received in revised form 15 March 2024; Accepted 13 April 2024

Available online 15 April 2024

1385-8947/© 2024 The Authors. Published by Elsevier B.V. This is an open access article under the CC BY-NC-ND license (<http://creativecommons.org/licenses/by-nc-nd/4.0/>).

Nomenclature (continued)

$h_{p,TubeBundle}$	particle-side heat transfer coefficient for staggered tube bundle ($W/m^2/K$)
$h_{HX,tot}$	total heat transfer coefficient ($W/m^2/K$)
$H_{bed,i}$	height of the bed (m)
$H_{p,in,i}$	inlet particle enthalpy (J/kg)
$H_{p,out,i}$	outlet particle enthalpy (J/kg)
$H_{g,in,i}$	inlet fluidized gas enthalpy (J/kg)
$H_{g,out,i}$	outlet fluidized gas enthalpy (J/kg)
i	number of the i^{th} stage
k_g	thermal conductivity of the gas ($W/m/K$)
k_{tube}	thermal conductivity of the tube ($W/m/K$)
$k_{p,CARBO}$	thermal conductivity of the CARBO particle ($W/m/K$)
$k_{p,CaO - based}$	thermal conductivity of the CaO-based particle ($W/m/K$)
k_s	chemical reaction rate constant ($m^4/mol/s$)
k_0	prefactor of the chemical reaction ($m^4/mol/s$)
K_s	ratio of the chemical reaction rate to the surface diffusion rate (-)
l_{top}	distance between the tubes in the upper row and the FB top surface (m)
l_{bot}	distance between the tubes in the lower row and the gas distributor (m)
l_d	horizontal gap between the tube centers (m)
l_h	vertical gap between the tube centers (m)
l_{wall}	minimum horizontal gap between the walls and close tubes (m)
$L_{tube,i}$	length of the tube (m)
$L_{bed,i}$	length of the bed (m)
$L_{tube,tot}$	total length of the tube (m)
$\dot{m}_{sCO_2, zigzag,i}$	mass flow of the zigzag tube (kg/s)
$\dot{m}_{sCO_2,i}$	mass flow of the sCO ₂ (kg/s)
$\dot{m}_{CO_2,in,i}$	inlet mass flow of the fluidized gas (kg/s)
$\dot{m}_{CO_2,out,i}$	outlet mass flow of the fluidized gas (kg/s)
$\dot{m}_{CO_2,abs,i}$	reactive gas (kg/s)
$\dot{m}_{p,out,i}$	outlet mass flow of the particle (kg/s)
$\dot{m}_{p,in,i}$	inlet mass flow of the particle (kg/s)
M_{CaO}	molar mass of CaO (kg/mol)
M_{CO_2}	molar mass of CO ₂ (kg/mol)
n_b	number of tube segments
$n_{tube,i}$	overall number of tubes
N_i	number of zigzags (-)
N_f	fluidization number (-)
$Nu_{p,i}$	Nusselt number (-)
p_{min}	minimum pitch (m)
$p_{diagonal}$	diagonal pitch (m)
p_D	geometric model function (-)
P_{sCO_2}	CO ₂ partial pressure (kPa)
$Pr_{sCO_2,i}$	sCO ₂ Prandtl number (-)
$\dot{Q}_{g,CO_2,i}$	fluidized gas heat transfer rate (W)
$\dot{Q}_{sCO_2,i}$	sCO heat transfer rate (W)
$\dot{Q}_{R,i}$	reaction release heat transfer rate (W)
$\dot{Q}_{p,i}$	particle heat transfer rate (W)
$r_{tube,in}$	internal tube radius (m)
$Re_{sCO_2,i}$	sCO ₂ Reynolds number (-)
$Re_{g,i}$	fluidization gas Reynolds number (-)
R_g	universal gas constant (J/(mol.K))
R_0	particle radius (μm)
$S_{horizontal}$	dimensionless parameters (-)
$S_{diagonal}$	dimensionless parameters (-)
S_0	initial surface area of CaO per unit volume of the solid particle (m^2/m^3)
$S_{bottom,i}$	bottom cross-sectional area (m^2)
t	time (s)
t^*	threshold time (s)
$T_{g,CO_2,in}$	inlet temperature of the fluidized gas (K)
$T_{p,out,i}$	outlet temperature of the particle (K)
$T_{p,in,i}$	inlet temperature of the particle (K)
$T_{sCO_2,in,i}$	inlet temperature of sCO ₂ (K)
$T_{sCO_2,out,i}$	outlet temperature of sCO ₂ (K)
$T_{sCO_2,mean,i}$	mean temperature of sCO ₂ (K)
$\Delta T_{mean,i}$	log-mean temperature difference between the hot particles and the cold sCO ₂
$T_{HX,max}$	maximum temperature of the heat exchanger (K)
$\bar{u}_{sCO_2,i}$	sCO ₂ velocity (m/s)
$u_{mf,i}$	minimum fluidization velocity (m/s)
$\bar{u}_{g,i}$	gas velocity (m/s)

(continued on next column)

Nomenclature (continued)

$U_{overall,i}$	overall heat transfer coefficient ($W/m^2/K$)
$V_{bed,i}$	fluidized bed volume (m^3)
V_R^M	molar volume of reactant CaO (m^3/mol)
V_P^M	molar volume of product CaCO ₃ (m^3/mol)
$W_{bed,i}$	weight of the bed (m)
Y_p	mass fraction of particle [-]
$Y_{CaO,initial}$	initial CaO mass fraction of particle [-]
$Y_{limestone,CaO,initial}$	initial CaO mass fraction of limestone (-)
$Y_{raw\ meal,CaO,initial}$	initial CaO mass fraction of the raw material (-)
$Y_{modified\ material,CaO,initial}$	initial CaO mass fraction of the modified material (-)
$Y_{CaO,i}$	CaO mass fraction of particles (-)
$Y_{CaCO_3,i}$	CaCO ₃ mass fraction of particles (-)
$Y_{inert,i}$	inert component mass fraction of particles (-)
Z	ratio of the molar volume of the solid product to that of the solid reactant (-)
Greek symbols	
α	degree of conversion (-)
$\bar{\alpha}_i$	average degree of conversion (-)
$\alpha_{tot,i}$	total degree of conversion (-)
β	model parameter (-)
γ_p	volume fraction of the particles in the reactor stage (-)
δ	fraction of unoccupied CaO area (-)
ϵ_0	initial porosity (-)
κ_s	geometric model function (-)
$\eta_{gas,loss}$	ratio of the fluidized gas heat transfer rate to the sCO ₂ transfer heat transfer rate (-)
η_{HEX}	global efficiency (-)
$\mu_{g,i}$	gas viscosity (Pa s)
ν_p	stoichiometric coefficient of product CaCO ₃ (-)
ν_R	stoichiometric coefficient of reactant CaO (-)
ξ	internal wall roughness of the tube (m)
$\rho_{g,i}$	gas density (kg/m^3)
$\rho_{p,out,i}$	outlet particle density (kg/m^3)
$\bar{\rho}_{sCO_2,i}$	density of sCO ₂ (kg/m^3)
$\rho_{p,CARBO}$	CARBO particle density (kg/m^3)
$\rho_{p,CaO}$	CaO particle density (kg/m^3)
$\rho_{p,CaCO_3}$	CaCO ₃ particle density (kg/m^3)
$\rho_{p,inert}$	doped inert material density (kg/m^3)
τ_p	mean residence time of the particles in a stage (s)
ϕ_p	particle sphericity (-)
ψ_p	particle sphericity (dimensionless)
Abbreviations	
FB	fluidized bed
HX	heat exchanger
CSP	Concentrated Solar Power
sCO ₂	supercritical carbon dioxide
PV	photovoltaics
TES	thermal energy storage
TCES	thermochemical energy storage
CaL	Calcium looping
SH	sensible heat
CSH	chemical and sensible heat

1. Introduction

Solar energy is an abundant renewable resource on the Earth, with approximately 430 EJ of energy from the sun reaching the Earth every hour; this value is nearly equal to the global total annual energy consumption [1]. The two main approaches for harnessing solar energy include thermal processes and electricity generation. Thermal processes involve the conversion of solar energy into heat for a wide range of applications, such as solar dryers, domestic hot water heating, water desalination, solar cooling, industrial process heating, and even thermochemical fuel production [2–4]. Electricity generation can be achieved through direct solar-to-electricity conversion by photovoltaics (PVs) and solar-to-heat and heat-to-electricity transformations by concentrated solar power (CSP) [5–8]. Although PV technology has experienced more widespread adoption and lower costs than CSP technology to date without considering energy storage, solar thermal power offers several advantages over PV, particularly for large-scale electricity generation and long-term energy storage. One of the most notable benefits of solar thermal power is its ability to utilize thermal energy

storage (TES) in CSP plants, effectively addressing the inherent challenge of solar intermittency [9–11]. In contrast, massive electrochemical storage for PV systems is too expensive to date, which hinders the integration of energy storage technology with PV installations [12].

Energy storage is a crucial component in enhancing the performance of CSP systems to mitigate the inherently intermittent effects of solar energy. There are three main types of TES technologies available: sensible, latent, and thermochemical energy storage (TCES) [13–15]. In recent years, interest has grown for thermochemical energy storage since this technology offers the highest specific energy density [10,16,17]. TCES offers several advantages over sensible and latent methods, including (i) high energy storage density, (ii) the ability to store energy over long periods without significant losses, and (iii) high operating temperature (reaching 1273 K). Among TCES systems, the calcium looping (CaL) process has attracted significant attention since calcium carbonate (CaCO_3) is widely available at a very low cost and is environmentally friendly [18]. In the CaL process, concentrated solar energy is used to carry out the endothermic CaCO_3 decomposition reaction to form calcium oxide (CaO) and carbon dioxide (CO_2) during sunlight hours [19–21]. When needed, CaO and CO_2 from two storage tanks are recombined to release thermal energy, as shown in Fig. 1(a). This heat can be utilized to drive a power cycle, such as a steam Rankine

cycle or a supercritical CO_2 Brayton cycle [22].

Research on high-temperature CaL energy storage systems is in its nascent stages, with the primary focus being on the development and evaluation of appropriate materials [16,23–25]. To date, numerous laboratory-scale investigations have been published, employing fluidized bed or centrifugal reactors to assess these materials and reactions [26–29]. In the 1980 s, Flamant et al. proposed a fluidized bed batch reactor using mixed silica and limestone particles with a chemical efficiency of 20 % [30]. Recently, Tregambi et al. investigated the CaL process for TCES by creating a solar-driven fluidized bed for CaL-CSP integration [31]. Facing the decrease in CaO conversion with time, the authors assessed the potential for segregating converted and unconverted particles after the carbonation step, leveraging the difference in particle density. German Aerospace Center has conducted many tests in recent years in solar rotary kilns, such as the calcination of kaolin at 700–1000 °C under a solar simulator [32,33]. Zheng et al. tested doped Ca-based pellets in a fluidized bed under direct solar irradiation to solve the issue of decreasing reactivity under cycling conditions [28]. A stable long-term Ca-based material has been developed, with an interpretation of the mechanisms underlying its superior cyclic and fast decomposition performance. The solar-thermal conversion efficiency of $(\text{AlMgFeMn})\text{O}_x\text{CaCO}_3$ pellets is significantly improved from 9 % to 19 % with respect

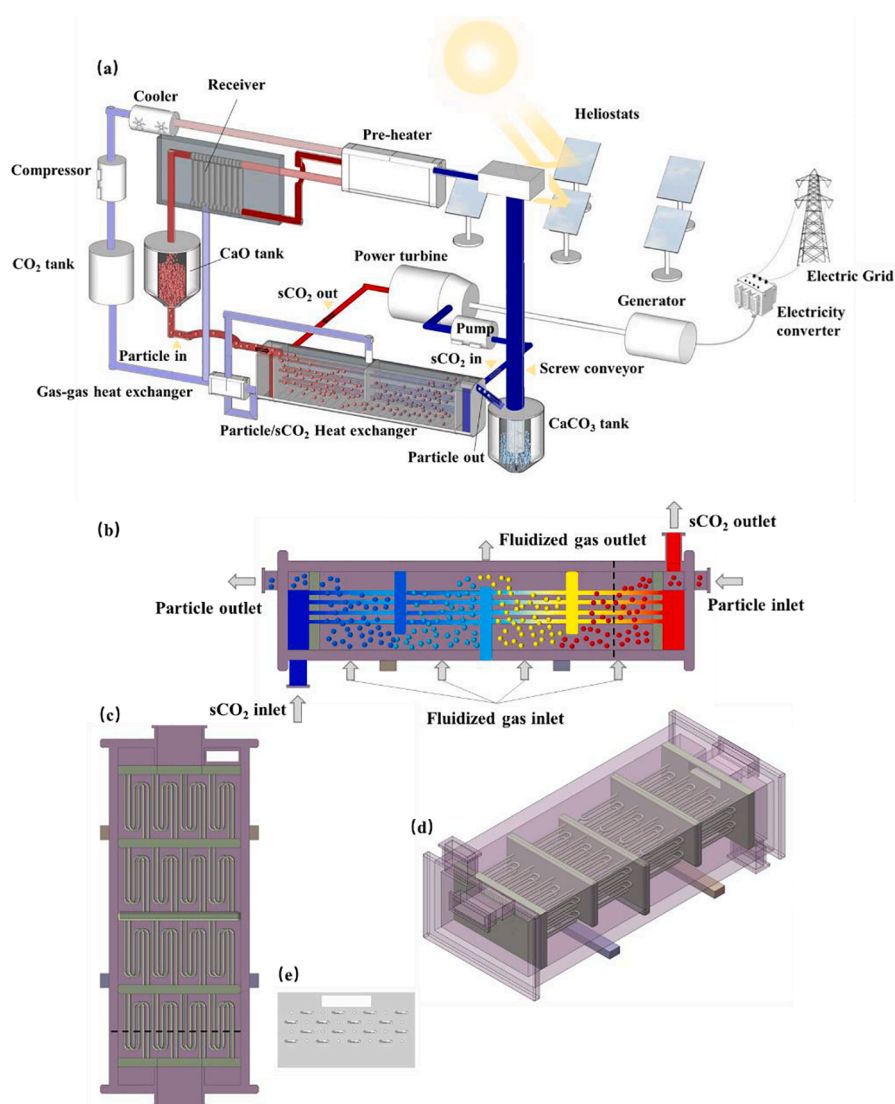


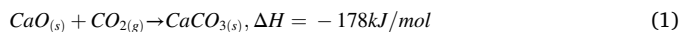
Fig. 1. (a) Schematic of a high-temperature calcium looping energy storage system with an sCO_2 Brayton power cycle, schematic diagram of the fluidized bed heat exchanger, (b) front view cross-section, (c) overhead cross-section, (d) overall schematic diagram, and (e) zigzag pipe arrangement cross-section.

to that of $(\text{AlMg})\text{O}_x\text{CaCO}_3$ pellets owing to considerably enhanced average solar absorption and fast reaction kinetics. However, the application of these concepts at the industrial scale is still challenging, and additional research and development must be undertaken, specifically targeting the following areas: (i) ensuring long-term performance of materials, including thermomechanical properties and stability under cycling conditions, (ii) choosing and designing CaCO_3 calcination reactors, and (iii) incorporating the CaO carbonation reactor (namely, the carbonator) into the power cycle [2,9,17]. This later aspect is addressed in this paper since it has been poorly studied by previous authors. In this component, the exothermal reaction between solid CaO particles and gaseous CO_2 provides heat to the conversion cycle at the desired temperature.

CaL-based TCES presents a compelling storage alternative to traditional molten salt due to its stability, cost-effectiveness, and ability to operate at temperatures exceeding 1023 K; molten salt can only operate at a maximum temperature of ~ 838 K [9]. The ability to operate at high temperatures not only increases the overall efficiency of the CSP plant but also matches well with the advanced sCO_2 Brayton cycle, in which turbine inlet temperature and pressure require values approaching 973 K and 20 MPa, respectively [34,35]. The sCO_2 Brayton cycle operates by using sCO_2 as the working fluid, which exhibits unique thermodynamic properties in the supercritical state, resulting in better cycle efficiency than traditional steam-based Rankine cycles (approximately 50 % relative to 43 %). A sCO_2 Brayton cycle system features a lower weight and volume, lower thermal mass, and a less complex power block than steam Rankine cycles due to the higher density of the fluid and the more streamlined cycle design. The compactness and high efficiency of the power block make the sCO_2 Brayton cycle appealing for the scales and temperature ranges associated with subsequent CSP generation. Nevertheless, attempts to merge the particle thermal storage system with the sCO_2 Brayton cycle must address the temperature, efficiency, and cost challenges faced by molten salt CSP systems to date [36,37].

In reactor design, the gas–solid reaction kinetics dictates the rate and magnitude of energy release within the reactor, and the heat transfer intensity between the particles and the exchanger surface governs the exchange area and the reactive medium temperature. Kinetic models for simulating CaO carbonation are generally divided into two categories: the shrinking-core-based grain model and the shrinking-pore-based random pore model [38–40]. However, both models are unable to predict the transition from the initial fast chemical reaction-controlled step to the relatively slow diffusion-controlled step or to simulate the effects of temperature on the transition behaviors. In contrast, Li et al. developed a general model that describes the complete kinetics of gas–solid reactions and validated it by experimental data [41]. This approach was selected in this study.

Fig. 1 presents an option for the coupling of a closed sCO_2 power cycle with a CSP system; other options can be found in Ref. [9]. During the charging process in the particle receiver, CaCO_3 particles are first decomposed into CaO and CO_2 . The hot CaO particles are then sent to the hot storage tank, while the hot CO_2 is used to preheat the cold CaCO_3 particles coming from the cold storage bin. The CO_2 from the preheater is cooled and compressed before being stored in a tank. It is used as a fluidizing gas in the FB HX. During the discharging process, the hot CaO particles flow into the reactive particle-to- sCO_2 shell and tube heat exchanger. In the heat exchanger, there are two CO_2 flows. The first one fluidizes the particles in the FB HX and is in direct contact with the particles. The second circulates inside the tube is the supercritical state. This flow has no contact with the particles. This working medium (sCO_2) is heated by the particles as part of the closed Brayton cycle. The associated reaction is as follows (1):



The particles are subsequently gathered in an insulated storage bin designed for low temperature (cold storage bin). Finally, an insulated

particle lifting mechanism transports the particles back to the top of the receiver. The connection between the particle thermal system and the sCO_2 Brayton cycle in a CSP plant is established through a particle-to- sCO_2 heat exchanger.

Several particle-to- sCO_2 heat exchangers, including moving packed beds and fluidized beds, have been investigated for power generation and chemical processes [34,42–46]. Among these systems, fluidized bed heat exchangers are an efficient and suitable technology for high-temperature TES applications. Weast and Shannon assessed the technical feasibility of FB HXs for TES systems in 1980 [43]. The authors identified and analyzed the operating characteristics and economics of FB HX systems for waste heat recovery and utilization. Farag et al. developed a mathematical model to solve the equations for counter-current and crosscurrent contacting multiple fluidized beds [44]. Ma et al. designed a fluidized bed of nonreactive particles. The authors presented a heat transfer model to analyze the particle- sCO_2 HX design and assessed design tradeoffs [34]. Gomez-Garcia et al. modeled a countercurrent multistage fluidized bed heat exchanger integrated with a steam Rankine cycle [45]. To our knowledge, none of the previous authors designed a fluidized bed heat exchanger with a chemical reaction for releasing the stored thermochemical energy in sCO_2 -CSP systems.

A detailed model of counter-flow shell and tube fluidized bed reactive heat exchangers was proposed. Single and multistage designs have been compared. Moreover, the tube length necessary to extract the same thermal power in the heat exchangers was compared for two thermal storage methods: only sensible heat storage and combined sensible and thermochemical energy storage. Heat transfer in the particles and the sCO_2 sides and the reaction kinetics were both presented. Furthermore, a sensitivity analysis was conducted to examine the impact of the key operating parameters on the variation in the inlet temperature of the sCO_2 working fluid, which is essential for understanding the operational stability and efficiency of the sCO_2 Brayton cycle.

2. Modeling of reactive fluidized bed heat exchangers

2.1. Heat exchanger description

The feasibility of multistage fluidized beds has been demonstrated in the context of continuous physical and chemical operations [43,45]. The analysis of the particle-to- sCO_2 FB HX incorporates established information on the gas and particle kinetic and thermal properties of reacting species, bed-to-tube and tube-to- sCO_2 heat exchange coefficients, and operational constraints. The proposed multistage FB HX is oriented horizontally, which is particularly suitable for endothermic and exothermic gas–solid reactions at high temperatures and particle circulation [47]. In each stage, fluidizing CO_2 is injected through perforated tubes located at the bottom of the reactor and particles fluidize through a uniform gas stream, inducing vigorous agitation of the particles. This agitation results in a homogenous temperature within the fluidized bed, fostering highly efficient heat transfer between the hot fluidized particles and the immersed tubes. The hot gas then exits the heat exchanger from the top, and it heats the fresh fluidized gas through an external gas heat exchange, this component was not introduced in the simulation.

The heat release processes in FB HXs featuring only sensible heat storage and featuring combinations of thermochemical and sensible heat storage systems were compared. A constant temperature difference of 150 K was assumed between the outlet and the inlet temperatures of sCO_2 , and the design was performed for a thermal power of 1-MW_t. A 150 K temperature difference matches the temperature of the heat necessary to supply an efficient sCO_2 cycle [48,49]. During the sensible heat release process, particles at 1048 K enter the heat exchanger, while fluidizing CO_2 enters from the bottom of the heat exchanger (CO_2 was selected as the fluidized gas to facilitate the comparison with the reactive case, and the calculation using air as the fluidized gas gave a similar

required inlet sCO₂ temperature of with a 12.8 K difference), ensuring uniform fluidization of the hot particles. The hot gas then exits the heat exchanger from the top. The sCO₂ working fluid is delivered to the conversion cycle at the suitable temperature. For the combined sensible and thermochemical heat release process, high-temperature particles enter the heat exchanger, along with the fluidizing gas, which serves as the reactive gas. This reactive gas reacts with the solid particles. The sensible and reaction heat is transported by the sCO₂ working fluid. Fig. 2 shows the frontal and sectional views of the single-stage heat exchanger without the insulation layer. To control the velocity of sCO₂, zigzag tubes have been used to ensure that it was maintained at approximately 3 m/s. The zigzags of each layer are staggered, the distance between the zigzags and the wall is l_{wall} , the distance between the zigzags and the top of the fluidized bed is l_{top} , the distance between the zigzags and the air distributor is l_{bot} , the distance between the two tubes is l_d , and the distance between the two layers of zigzags is l_h . sCO₂ is distributed to all zigzags simultaneously, and the sCO₂ at the exit of each stage is collected again and distributed to the zigzags of next stage as shown in Fig. 1(c) and (d).

Table 1 presents a list of the performance targets for a 1-MWt heat exchanger, and Table 2 displays the primary input parameters for the model. Except for $c_{p,\text{CARBO}}$ and c_{p,CaCO_3} , which were based on the outlet temperature of particles in the FB HX, other parameters were fixed. The parameters in Table 2 are the basic parameters used to start the optimization process in section 3.1 and 3.2. The basic parameters were also used in the sensitivity analysis in section 3.3, except the key variables $D_{\text{tube,in}}$ and $D_{\text{tube,out}}$.

According to the experimental results of Esence et al., in the calcination process of CaCO₃ under solar irradiation, the material temperature can reach an average bed temperature between 1063 and 1104 K [29]. In the simulation, the heat loss in the storage process was considered and set the particle inlet temperature to 1043 K. Conversely, high-efficiency sCO₂ power cycles necessitate conditions of high

Table 1

Target performance metrics for each FB HX.

Target Metrics	Value	Unit
Thermal duty	0.99–1.07	MW _{th}
$h_{\text{HX,tot}}$	400–450	W/m ² /K
$T_{\text{HX,max}}$	1100	K
$T_{p,\text{in},1}$	1048	K
$T_{p,\text{out}}$	< 853	K
$T_{\text{sCO}_2,\text{in},1}$	< 838	K
$T_{\text{sCO}_2,\text{out}}$	988	K
P_{sCO_2}	20	MPa
$\dot{m}_{\text{sCO}_2,\text{in},1}$	5.26	kg/s
$\bar{\alpha}_{\text{tot}}$	> 0.97	–

pressure (≥ 20 MPa) and high temperature (≥ 973 K). Therefore, the working fluid pressure and outlet temperature values were fixed at 20 MPa and 988 K, respectively. The expected conversion of the reactive material in the FB HX was higher than 95 %. In this study, the sCO₂ inlet temperature was set as a variable to reach the targeted outlet temperature of sCO₂ (988 K), which is the most important parameter for evaluating the sCO₂ cycle performance.

2.2. Heat transfer model

The convective heat transfer rate transferred from the particles to the working fluid within each stage of the HX is described by the following equation:

$$\dot{Q}_{\text{sCO}_2,i} = U_{\text{overall},i} A_{\text{tube},i} \Delta T_{\text{mean},i} \quad (2)$$

where $A_{\text{tube},i} = \pi D_{\text{tube}} L_{\text{tube},i}$ is the wetted surface area of the tubes in the heat exchanger. Therefore, $U_{\text{overall},i} A_{\text{tube},i}$ represents the thermal resistance, which is calculated as follows:

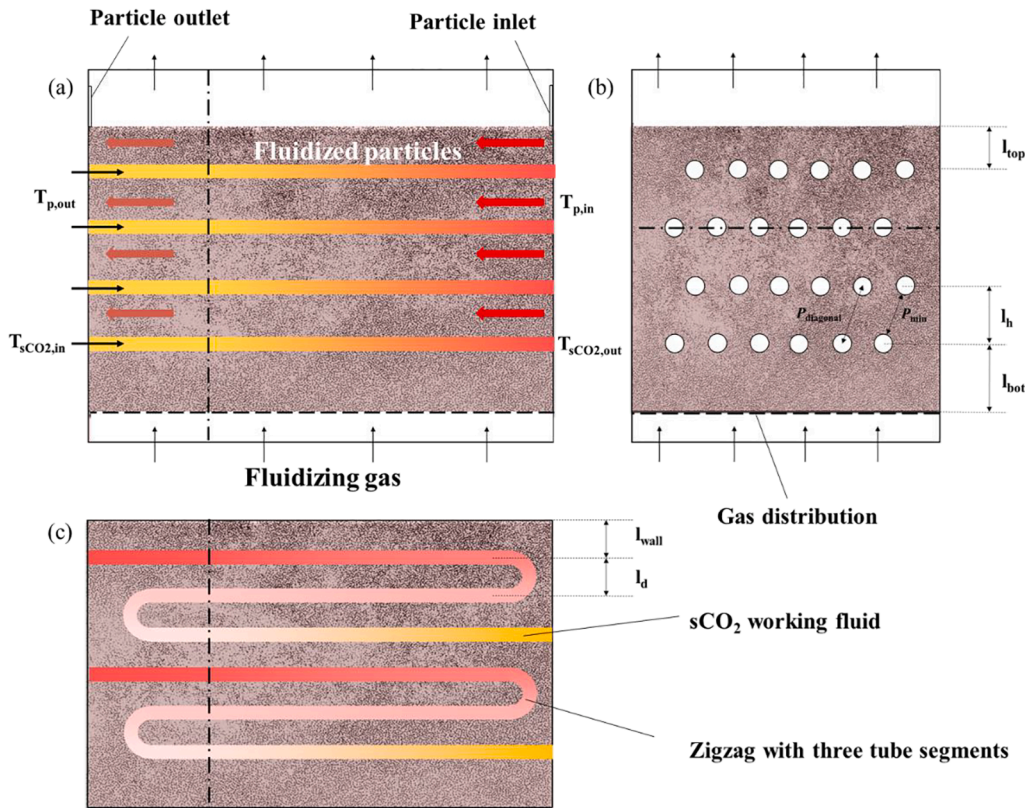


Fig. 2. Frontal view (a), lateral sectional view (b), and top sectional view (c) of the particle/sCO₂ FB HX. N zigzag tubes are considered, with each being composed of segments.

Table 2
Input values for the model.

Parameter	Value	Unit
l_{top}	50	mm
l_{bot}	100	mm
$D_{tube,out}$	25.4	mm
$D_{tube,in}$	20.4	mm
l_d	$3.15 * D_{tube,out}$	mm
l_h	$2.75 * D_{tube,out}$	mm
l_{wall}	$3.15 * D_{tube,out}$	mm
ξ	2	μm
κ_{tube}	15	W/m/K
d_p	100	μm
φ_p	0.9	–
$\rho_{p,CARBO}$	3300	kg/m^3
$\rho_{p,CaO}$	3340	kg/m^3
$\rho_{p,CaCO_3}$	2700	kg/m^3
$\rho_{p,inert}$	3040	kg/m^3
$Y_{limestone,CaO,initial}$	0.987	–
$Y_{raw\ material,CaO,initial}$	0.52	–
$Y_{modified\ material,CaO,initial}$	0.8	–
γ_p	0.45	–
$C_{p,CARBO}$	$365 * T_{p,out}^{0.18}$	J/mol/K
$C_{p,CaCO_3}$	$104.52 + 21.92 * 10^{-3} * T_{p,out} - 2.59 * 10^{-6} * T_{p,out}^2$	J/mol/K
N_f	5	–
$T_{g,CO_2,in}$	293	K

$$U_{overall,i} A_{tube,i} = \frac{1}{\frac{1}{h_{sCO_2,i} \pi D_{tube,out} L_{tube}} + \frac{1}{h_{p,i} \pi D_{tube,in} L_{tube}} + \frac{\ln(D_{tube,out}/D_{tube,in})}{2\pi \kappa_{tube} L_{tube}}} \quad (3)$$

$\Delta T_{mean,i}$ is the log-mean temperature difference between the hot particles and the cold sCO₂, and it is calculated as follows:

$$\Delta T_{mean,i} = \frac{(T_{p,in,i} - T_{sCO_2,out,i}) - (T_{p,out,i} - T_{sCO_2,in,i})}{\ln\left\{\frac{(T_{p,in,i} - T_{sCO_2,out,i})}{(T_{p,out,i} - T_{sCO_2,in,i})}\right\}} \quad (4)$$

The particle and sCO₂ temperature calculation process in each stage can be found in Fig. S1 of Supporting Information.

2.2.1. sCO₂ side heat transfer coefficient

The fluid velocity inherently governs the heat transfer coefficient on the sCO₂ side. The sCO₂ working fluid velocity depends on the heat exchanger tube internal diameter and the sCO₂ mass flow rate $\dot{m}_{sCO_2,b,i}$. The velocity is calculated as follows:

$$\bar{u}_{sCO_2,i} = \frac{\dot{m}_{sCO_2,b,i}}{\rho_{sCO_2,i} \pi r_{tube,in}^2} \quad (5)$$

$$\dot{m}_{sCO_2,b,i} = \frac{\dot{m}_{sCO_2,i}}{N_i} \quad (6)$$

where N_i is the number of zigzags and $\dot{m}_{sCO_2,i}$ is set as 5.26 kg/s based on the required thermal duty. $\rho_{sCO_2,i}$ is the sCO₂ density according to the average temperature of the inlet and outlet of sCO₂. The sCO₂ heat transfer coefficient can be optimized by modulating the flow velocity $\bar{u}_{sCO_2,i}$, which is achieved by adjusting the number of tube segments n_b in each zigzag. The overall number of tubes in the stage can be given as: $n_{tube,i} = n_b N_i$. The local convective heat transfer coefficients for sCO₂ are calculated using the Gnielinski correlation, which is a well-established method for determining turbulent flow in tubes ($Re_{CO_2} > 3000$) [50,51],

$$Nu_{sCO_2,i} = \frac{(f_i/8)(Re_{sCO_2,i} - 1000)Pr_{sCO_2,i}}{1 + 12.7(f_i/8)^{1/2}(Pr_{sCO_2,i}^{2/3} - 1)} \quad (7)$$

$$\frac{1}{\sqrt{f_i}} = -2 \log\left(\frac{\xi/D_{tube,in}}{3.7} + \frac{2.51}{Re_{sCO_2} \sqrt{f_i}}\right) \quad (8)$$

The thermal-physical properties of the sCO₂ working fluid are calculated by referencing the NIST standard database [52]. The thermal characteristics of the sCO₂ working fluid within each stage are determined based on the mean temperature, considering both inlet and outlet temperatures. As shown in Fig. 3(a), with the increase in the number of zigzag tubes and the increase in the inner diameter of the pipe, the mass flow rate of the tube decreases, resulting in a decrease in the heat transfer coefficient of the sCO₂ working medium. In contrast, with the increase in the temperature and pressure of sCO₂, the heat transfer coefficient of sCO₂ increases, as shown in Fig. 3(b).

2.2.2. Particle-side heat transfer coefficient

Particle-side heat transfer is the primary limiting factor influencing the performance of the heat exchanger. The heat transfer coefficient on the particle side is affected by the physical properties and size of the particle and the operating conditions of the heat exchanger. One of the main operating conditions of the heat exchanger is the minimum fluidization velocity, which is expressed as follows [53]:

$$u_{mf,i} = \frac{\bar{\mu}_{g,i} Re_{g,i}}{\bar{\rho}_{g,i} d_p} \quad (9)$$

$$Re_{g,i} = \sqrt{31.6^2 + 0.0425 Ar_{g,i}} - 31.6 \quad (10)$$

The gas velocity in a stage is determined as follows:

$$\bar{u}_{g,i} = N_f u_{mf,i} \quad (11)$$

The particle size employed in this study is 100 μm , which closely aligns with the range of 112–2125 μm applicable to Eq. (9). Hence, Eq. (9) was adopted in this study. Fig. 3(c) presents a plot of the effects of particle size and temperature on the minimum fluidization velocity. A relatively conservative fluidization number, $N_f = 5$, was chosen because it ensures a high bed-to-tube heat transfer coefficient while minimizing the particle-induced erosion of heat exchanger tubes. In heat exchangers, for thermochemical and sensible heat release, the additional absorbed gas introduced serves to fluidize the particles. This strategy prevents the fluidized bed from becoming static due to CO₂ consumption by CaO reacting particles. Therefore, the fluidized gas mass flow is expressed as follows:

$$\dot{m}_{CO_2,in,i} = \rho_{g,i} \bar{u}_{g,i} S_{bottom,i} + \dot{m}_{CO_2,abs,i} \quad (12)$$

where $\dot{m}_{CO_2,abs,i}$ is the mass flow of CO₂ absorbed by particles and $S_{bottom,i}$ is the bottom cross-sectional area of the heat exchanger. The inlet fluidized gas and absorbed gas are CO₂ at a temperature of 293 K and pressure of 100 kPa. The outlet gas temperature in each stage is equal to the outlet solid temperature because the high mixing rate in FB results in a uniform temperature throughout the bed according to Kunii et al [54,55]. The bed pressure drop was neglected throughout the bed. The thermal properties are calculated at the outlet gas temperature using the NIST standard database [52]. Since the model is focused on the heat balance inside the heat exchanger, the pressure drops inside the tubes and in the fluidized bed were not considered. They were estimated to 8.2 kPa for the tubes and to 46.6 kPa in the fluidized bed of the single stage with reaction.

The convective heat transfer coefficient between the tubes and the fluidized bed at any given stage is established in accordance with the results of Grewal and Saxena et al. [56]. Stenberg et al. experimentally validated the high accuracy of the Grewal and Saxena heat transfer

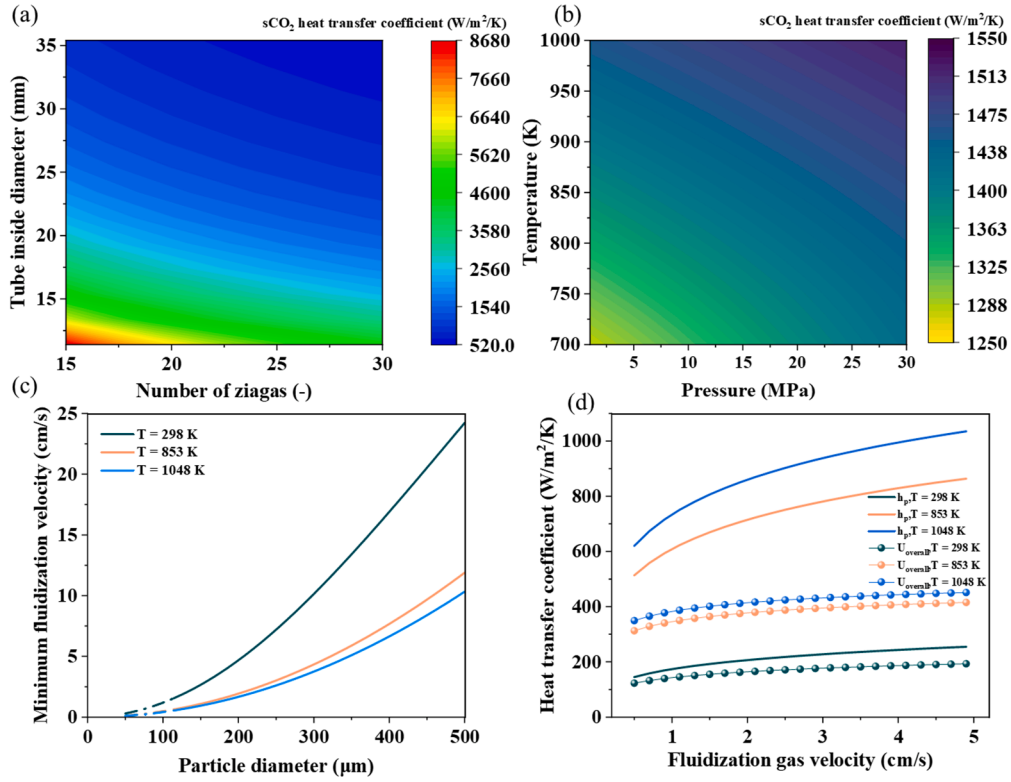


Fig. 3. sCO₂ side heat transfer coefficient versus (a) the number and outer diameter of zigzag tubes ($P = 20$ MPa, $T_{sCO_2,mean} = 920$ K), (b) mean sCO₂ temperature and pressure ($D_{tube,in} = 20.4$ mm, $N_i = 30$), (c) effects of particle size on minimum fluidization velocity at different temperatures ($\rho_p = 2700$ kg/m³), and (d) particle-side heat transfer coefficients and overall heat transfer coefficients versus the fluidization velocities at different temperatures ($d_p = 100\mu\text{m}$, $h_{sCO_2} = 1170\text{W/m}^2/\text{K}$, $\rho_p = 2700\text{kg/m}^3$, $D_{tube,in} = 20.4$ mm).

correlation for predicting heat transfer under high-temperature conditions [57]. The particle size used in this study is similar to that one tested by Grewal and Saxena et al. In their work, a general correlation was proposed considering various parameters, including the particle size, physical properties, and thermal properties; this correlation is expressed as follows:

$$Nu_{p,i} = 47(1 - \varepsilon) \left(\frac{\rho_{p,out,i} \bar{u}_{g,i} D_{tube,out}}{\bar{\mu}_{g,i}} \frac{\bar{P}_{g,i}^2}{d_p^3 \rho_{p,out,i}^2 g} \right)^{0.325} \left(\frac{\rho_{p,out,i} c_{p,s,i} D_{tube,out}^{3/2} g^{1/2}}{k_g} \right) \left(\frac{c_{p,g,i} H_g}{k_g} \right)^{0.3} \quad (13)$$

$$\varepsilon = \frac{1}{2} \left[0.4 + \left\{ 4 \left(\frac{\bar{u}_{g,i} \bar{\mu}_{g,i}^2}{d_p^2 \rho_{p,out,i} \phi_p^2 g} \right)^{0.43} \right\}^{1/3} \right] \quad (14)$$

The heat transfer performance of fluidized beds equipped with bundles of horizontal heat exchanger tubes was investigated by [58]. A decrease of the heat transfer coefficient was observed as a function of tube spacing. In order to account for this decrease a reduction factor was derived to define the extent of influence of the tube bundle arrangement on the mean fluidized bed-to-tube heat transfer coefficient. This reduction factor enables to calculate the decrease of the mean heat transfer coefficient between a single tube and tube bundles. The tube bundle reduction factor can be calculated as follows according to Lechner et al [58]:

$$f_{TB} = \left(1 - \frac{1}{s_{horizontal}} \right)^{0.36} \cdot \left(1 - \frac{1}{s_{diagonal}} \right)^{0.24} \cdot \left(1 - \frac{d_p}{p_{min}} \right)^4 \cdot \left(\frac{D_{tube,out}}{d_{22mm}} \right)^{0.09} \quad (15)$$

where $\left(1 - \frac{1}{s_{horizontal}} \right)^{0.36}$ is the factor ‘‘horizontal spacing’’, $\left(1 - \frac{1}{s_{diagonal}} \right)^{0.24}$ is the Factor ‘‘diagonal spacing’’, and $\left(1 - \frac{d_p}{p_{min}} \right)^4$ is the Factor ‘‘perme-

ability’’. There remain three dimensionless parameters are defined as $s_{horizontal} = \frac{l_d}{D_{tube,out}}$, $s_{diagonal} = \frac{p_{diagonal}}{D_{tube,out}}$, permeability = $\frac{d_p}{p_{min}}$. $D_{tube,out}$ and d_p are the tube diameter and particle diameter.

Consequently, the heat transfer coefficient for staggered tube bundle with respect to single tube is defined by,

$$h_p = h_{p,TubeBundle} = h_{p,singleTube} f_{TubeBundle} \quad (16)$$

In the fluidized bed heat exchanger configuration designed in this paper, l_d is $3.15 * D_{tube,out}$ and l_h is $2.75 * D_{tube,out}$. Therefore, the tube bundle reduction factor is $f_{TB} = 0.8$.

Fig. 3(d) presents a plot of the particle-side heat transfer coefficient for staggered tube bundle and overall heat transfer coefficient ($U_{overall}$) at different temperatures.

The density of the particles varies with the conversion and is calculated as follows:

$$\rho_{p,out,i} = y_{CaO,i}\rho_{p,CaO} + y_{CaCO_3,i}\rho_{p,CaCO_3} + y_{inert,i}\rho_{p,inert} \quad (17)$$

where the mass fraction of the components ($y_{CaO,i}$, $y_{CaCO_3,i}$, and $y_{inert,i}$) in the particles varies with the chemical conversion. The calculation process is shown in Fig. S2 of Supporting Information.

2.3. Reaction kinetics

The reaction kinetics of Ca-based materials are estimated by a general reaction rate equation, according to Li et al. [41]. The general equation considers the rate transitions from the initial fast chemical reaction-controlled step to the subsequent slow diffusion step and the influence of temperature on the kinetics of these transitions. The equation is described as follows:

$$\frac{d\alpha}{dt} = \frac{k_s S_0}{1 - \varepsilon_0} \kappa_s (C - C_c) \left(\frac{\delta}{1 + K_s (C - C_c)} + \frac{1 - \delta}{g_D + \beta (C - C_c) p_D} \right) \quad (18)$$

where $\beta = \frac{k_s(1-\varepsilon_0)}{V_R^M D_p S_0}$, $K_s = \frac{k_c Z}{D_s}$, and $Z = \frac{\nu_p V_p^M}{\nu_R V_R^M}$; ν_R and ν_p are the stoichiometric coefficients of the reactant and the product, respectively; V_R^M and V_p^M are the molar volumes of the reactant and the product, respectively; and κ_s , g_D , and p_D are all geometric model functions. The spherical grain model was used to investigate the carbonation kinetics. Therefore, the geometric model function is described as follows:

$$\kappa_s = (1 - \alpha)^{\frac{2}{3}} \quad (19)$$

$$g_D = \frac{(1 - \alpha)^{\frac{2}{3}}}{[1 + \alpha(\frac{Z}{(1-\delta)} - 1)]^{\frac{2}{3}}} \quad (20)$$

$$p_D = \frac{3(1 - \alpha)^{\frac{1}{3}}}{\{1 + \alpha[\frac{Z}{(1-\delta)} - 1]\}^{\frac{2}{3}}} \{ [1 + \alpha(\frac{Z}{(1-\delta)} - 1)]^{\frac{2}{3}} - (1 - \alpha)^{\frac{1}{3}} \} \quad (21)$$

where δ is the unoccupied reactant surface. The change in δ with time can be expressed as follows:

$$\frac{d\delta}{dt} = \frac{k_s}{D_s} \frac{C - C_c}{1 + K_s (C - C_c)} \delta \quad (22)$$

where $C_c = \frac{1.826 \times 10^6}{8.314 T_{p,out,i}} \exp(-\frac{19680}{T_{p,out,i}})$ in the CaO carbonation process according to the Hu et al. results [59] and C is the concentration of reacting gas inside the particle. The kinetic parameters are written in the Arrhenius equation form:

$$k_s = k_0 \exp(-\frac{E_k}{R_g T_{p,out,i}}) \quad (23)$$

$$D_s = D_{s0} \exp(-\frac{E_s}{R_g T_{p,out,i}}) \quad (24)$$

$$D_p = D_{p0} \exp(-\frac{E_p}{R_g T_{p,out,i}}) \quad (25)$$

Table 3
Input values for the model.

	Raw material	Limestone	Modified materials
S_0	4.29*10 ⁶	4.2*10 ⁷	1.525*10 ⁷
ε_0	0.661	0.47	0.487
R_0	49	63–100	50–75
x_{CaO}	52 %	99 %	80 %
k_{s0}	3.12*10 ⁻⁸	2.72*10 ⁻⁷	3.37*10 ⁻⁸
E_k	11.55	44.76	36.98
D_{p0}	5.06*10 ⁻⁸	7.72*10 ⁻¹⁰	7.82*10 ⁻¹³
E_p	93.44	80.21	26.46
D_{s0}	2.02*10 ⁻⁶	2.58*10 ⁻⁶	5.08*10 ⁻⁵
E_s	30.06	37.99	48.00

By separating the microstructural parameters (S_0 and ε_0), kinetic parameters (k_s , D_s , and D_p), product island growth model (δ), and geometric model (κ_s , g_s , and p_D), this formula can accurately predict the reaction rates at varying temperatures for different calcium-based materials. This equation is a useful analytical model for gas–solid reactor modeling.

In the fluidized bed heat exchanger, the characteristics of conversion versus time are compared for three calcium-based particles—the well-known and cost-effective natural limestone with a CaO content of 98.7 wt%, the cement raw material with a CaO content of 52 wt%, and the modified Al-doped materials with a CaO content of 80 wt%—recognized for their superior cyclic performance. Their pore structure parameters and kinetic parameters are outlined in Table 3 [39,41,60,61].

Based on Eq. (16), as time exceeds a certain limit (t^*), the conversion may be greater than 1. Thus, in such cases, the conversion was set to its maximum attainable value, which is 1 [27]. As each stage of the HX is assumed to be an ideal continuous stirred-tank reactor, the residence time distribution $E(t)$ for particles is described by Eq. (24) according to Rawlings and Ekerdt et al. [62]. Consequently, the average conversion at the stage outlet is determined by Eq. (25).

$$E(t) = \frac{1}{\tau_p} \exp(-\frac{t}{\tau_p}) \quad (26)$$

$$\bar{\alpha}_i = \int_{t=0}^{t=\infty} \alpha(t) E(t) dt = \int_{t=0}^{t=t^*} \alpha(t) E(t) dt + \int_{t=t^*}^{t=\infty} \alpha_{\max} E(t) dt \quad (27)$$

where τ_p is the mean residence time; this value will be discussed in the following section. Eq. (25) presents the conversion of the particles from the inlet to the outlet of a specific stage i .

The overall conversion, denoted as $\bar{\alpha}_{tot,i}$, is determined from the HX inlet to the outlet of stage i using Eq. (26). $\bar{\alpha}_{tot,0} = 0$ is set to 0 since no CaCO₃ is present at the reactor inlet.

$$\bar{\alpha}_{tot,i} = \bar{\alpha}_{tot,i-1} + \bar{\alpha}_i (1 - \bar{\alpha}_{tot,i-1}) \quad (28)$$

The solving procedure of the particles total average conversion is shown in Fig. S3. It is obtained by iterative calculation of reaction kinetics and particle outlet temperature.

2.4. Energy and mass balance

For the FB HX, the energy variation can be divided into three items: the heat transfer rate released from the particles, the heat transfer rate of the fluidized gas, and the heat transfer rate transported by the sCO₂. Here, the two-stage FB HX mathematical model (Fig. S1) is taken as an example to better represent the changes in energy and mass in the multistage fluidized bed, which is also applicable to the single-stage fluidized bed.

The heat transfer rate by the particles is given as follows:

$$\dot{Q}_{p,i} = \dot{m}_{p,out,i} H_{p,out,i} - \dot{m}_{p,in,i} H_{p,in,i} \quad (29)$$

where $H_{p,out,i}$ and $H_{p,in,i}$ is the inlet and outlet particle enthalpy.

The heat transfer rate by the fluidization gas is given by the following equation:

$$\dot{Q}_{g,CO_2,i} = \dot{m}_{g,out,i} H_{p,out,i} - \dot{m}_{g,in,i} H_{g,in,i} \quad (30)$$

where $H_{g,out,i}$ and $H_{g,in,i}$ is the inlet and outlet fluidized gas enthalpy.

In the release process with sensible heat (SH) only, as shown in Fig. S1(a), the energy balance equations are written as follows:

$$\dot{Q}_{sCO_2,1} + \dot{Q}_{g,CO_2,1} + \dot{Q}_{p,1} = 0 \quad (31)$$

$$\dot{Q}_{sCO_2,2} + \dot{Q}_{g,CO_2,2} + \dot{Q}_{p,2} = 0 \quad (32)$$

The mass flow rates of gas, particles and sCO₂ in the SH case do not change.

The heat release process from CaO particles is divided into two parts: sensible heat and heat from the chemical reaction. Therefore, the energy balance in the CaO carbonation process with chemical and sensible heat (CSH) is calculated by the following equations:

$$\dot{Q}_{sCO_2,1} + \dot{Q}_{R,1} + \dot{Q}_{g,CO_2,1} + \dot{Q}_{p,1} = 0 \quad (33)$$

$$\dot{Q}_{sCO_2,2} + \dot{Q}_{R,2} + \dot{Q}_{g,CO_2,2} + \dot{Q}_{p,2} = 0 \quad (34)$$

The particle mass flow rate at the outlet of each stage depends on the absorbed CO₂ mass flow. For the first stage, it is given by the following formula:

$$\dot{m}_{p,out,1} = \dot{m}_{p,in,1} + \bar{\alpha}_1 \frac{y_{CaO,initial} \dot{m}_{p,in,1}}{M_{CaO}} M_{CO_2} \quad (35)$$

where $y_{CaO,initial}$ is the initial mass fraction of reacting CaO. For the second stage, the particle mass flow rate is calculated as follows:

$$\dot{m}_{p,out,2} = \dot{m}_{p,in,1} + \bar{\alpha}_1 \frac{y_{CaO,initial} \dot{m}_{p,in,1}}{M_{CaO}} M_{CO_2} + \bar{\alpha}_2 \frac{y_{CaO,initial} \dot{m}_{p,in,1} (1 - \bar{\alpha}_{tot,1})}{M_{CaO}} M_{CO_2} \quad (36)$$

The heat transfer rate due to chemical reaction for the first stage is given by the following equation:

$$\dot{Q}_{R,1} = \bar{\alpha}_1 \frac{y_{CaO,initial} \dot{m}_{p,in,1}}{M_{CaO}} \Delta H \quad (37)$$

where ΔH is the reaction enthalpy with a value of -178 kJ/mol. The heat transfer rate by reaction release for second stage is given as follows:

$$\dot{Q}_{R,2} = \bar{\alpha}_2 \frac{y_{CaO,initial} \dot{m}_{p,in,1} (1 - \bar{\alpha}_{tot,1})}{M_{CaO}} \Delta H \quad (38)$$

The solving procedure of the heat balance related to the heat exchanger tube length is shown in Fig. S5 of SI. The fixed values are the inlet temperature of the particle ($T_{p,in,i}$) (flowing from the storage tank) and the outlet temperature of sCO₂ ($T_{sCO_2,out,i}$). The inlet temperature of the sCO₂ working medium ($T_{sCO_2,in,i}$) and the outlet temperature of the particles ($T_{p,out,i}$) are iterated repeatedly until convergence is reached. On the one hand, the logarithmic mean temperature difference $\Delta T_{mean,i,2}$ in each stage of the heat exchanger is determined, in which the variables to be determined is $T_{p,out,i}$. For the sCO₂ working fluid side, $T_{sCO_2,in,i}$ is determined by the sCO₂ heat transfer rate ($\dot{Q}_{sCO_2,i}$), and $T_{sCO_2,out,i}$ is assumed to be 988 K (fixed value) according to the Brayton cycle system requirements. $\Delta T_{mean,i,2}$ is the log-mean temperature difference between the hot particles and the cold sCO₂, which can be calculated by Eq. (4). On the other hand, once the tube-working medium convective heat transfer coefficient ($h_{sCO_2,i}$) and the particle-to-tube convective heat transfer coefficient ($h_{p,i}$) are determined, the total thermal resistance ($U_{overall,i} A_{tube,i}$) can be calculated, and, consequently, $\Delta T_{mean,i,1}$. Number 1 and 2 in the $\Delta T_{mean,i,1}$ and $\Delta T_{mean,i,2}$ are related to iteration 1 and iteration 2. By comparing the $\Delta T_{mean,i,1}$ and $\Delta T_{mean,i,2}$ for each stage, the heat exchanger tube length $L_{tube,tot}$ that meets the requirements ($T_{sCO_2,in,i} < 838$ K) is selected.

The fraction of energy loss in the fluidizing gas of the FB HX is evaluated by the following equation:

$$\eta_{gas,loss,i} = \frac{\dot{Q}_{g,CO_2,i}}{-(\dot{Q}_{R,i} + \dot{Q}_{p,i})} = \frac{\dot{Q}_{g,CO_2,i}}{\dot{Q}_{g,CO_2,i} + \dot{Q}_{sCO_2,i}} \quad (39)$$

$$\eta_{gas,loss,tot} = \frac{\sum_i \dot{Q}_{g,CO_2,i}}{-(\sum_i \dot{Q}_{R,i} + \sum_i \dot{Q}_{p,i})} = \frac{\sum_i \dot{Q}_{g,CO_2,i}}{\sum_i \dot{Q}_{g,CO_2,i} + \sum_i \dot{Q}_{sCO_2,i}} \quad (40)$$

The global heat exchanger effectiveness can be defined as the ratio of the difference between the sCO₂ and solid outlet temperatures to the dif-

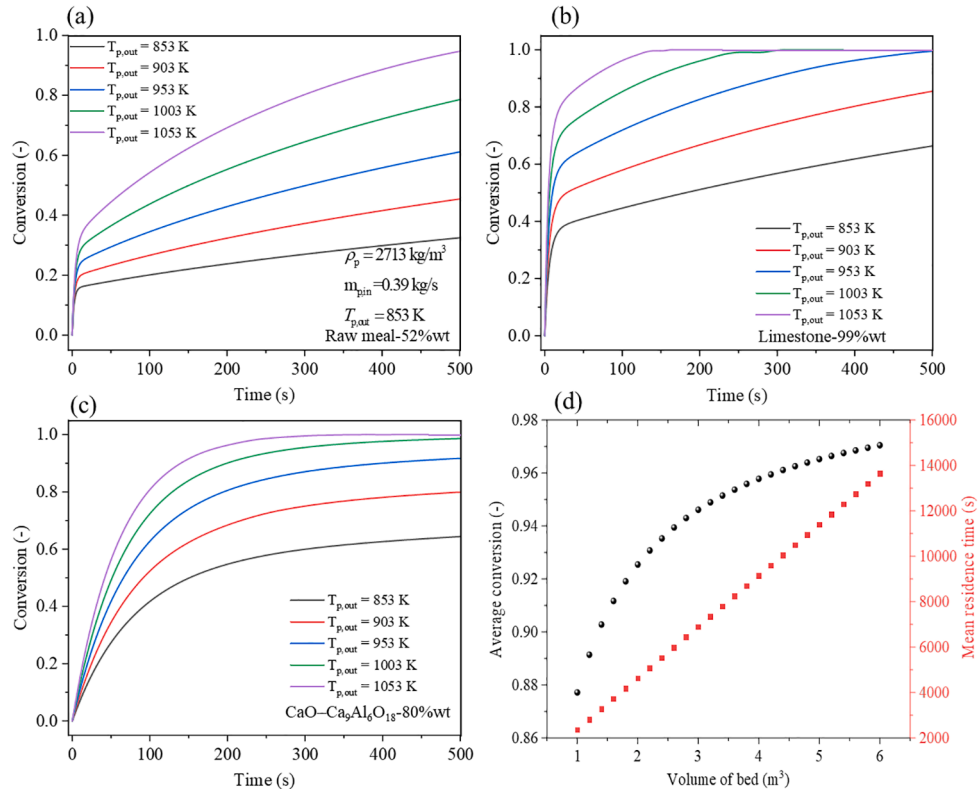


Fig. 4. Conversion–time plots at different temperatures: (a) raw material, (b) limestone, and (c) modified material. (d) Mean residence time and average conversion in one stage versus the volume of the fluidized bed (limestone).

ference between their inlet temperatures:

$$\eta_{\text{HEX}} = \frac{T_{\text{sCO}_2, \text{out}, 1} - T_{\text{p}, \text{out}, i}}{T_{\text{p}, \text{in}, 1} - T_{\text{sCO}_2, \text{in}, i}} \quad (41)$$

This is an indicator of the gap between the real system and an ideal one since if $T_{\text{sCO}_2, \text{out}, 1} = T_{\text{p}, \text{in}, 1}$ and $T_{\text{p}, \text{out}, i} = T_{\text{sCO}_2, \text{in}, i}$ the value of the indicator is one. Consequently, any real HX corresponds to an effectiveness less than one.

The mean residence time τ_p of fluidized particles within a stage is calculated as follows:

$$\tau_p = \frac{2\gamma_p \rho_{\text{p}, \text{out}, i} V_{\text{bed}, i}}{\dot{m}_{\text{p}, \text{in}, i} + \dot{m}_{\text{p}, \text{out}, i}} \quad (42)$$

where γ_p is the volume fraction of particles, $\rho_{\text{out}, i}$ is the outlet density of particles, and $V_{\text{bed}, i}$ is the volume of the fluidized bed in the stage.

Fig. 4(d) shows a plot of the mean residence time of the particle and the corresponding average conversion for the limestone as a function of the fluidized bed volume.

2.5. Cost analysis of the particle/sCO₂ heat exchanger using SH and CSH materials

The cost of the heat exchanger is mainly composed of three parts: heat exchanger tube cost, storage particle cost, and sCO₂ cost. The used correlations are calculated as follows according to the G3P3 project [63,64]:

$$C_{\text{HX}} = c_{\text{HX}, A} A_{\text{HX}} + c_{\text{BOP}, p} \dot{m}_{\text{p}, \text{in}} + c_{\text{BOP}, \text{sCO}_2} \dot{m}_{\text{sCO}_2, \text{in}} \quad (43)$$

where $c_{\text{BOP}, p} = 9153\$/(\text{kg}/\text{s})$ is the particle-side specific balance of the plant cost, $c_{\text{BOP}, \text{sCO}_2} = 4752\$/(\text{kg}/\text{s})$ is the sCO₂-side specific balance of the plant cost, and $c_{\text{HX}, A} = 9031\$/\text{m}^2$ is the value for the area-specific heat exchanger cost at 973 K. The required heat transfer area of the heat exchanger is as follows:

$$A_{\text{HX}} = \pi D_{\text{tube}, \text{out}} L_{\text{tube}, \text{tot}} \quad (44)$$

$$V_{\text{HX}} = \pi R_{\text{tube}, \text{in}}^2 L_{\text{tube}, \text{tot}} \quad (45)$$

where $D_{\text{tube}, \text{out}}$ is the outside surface diameter, $R_{\text{tube}, \text{in}}$ is the inside radius, and $L_{\text{tube}, \text{tot}}$ is the total tube length of the FB HX.

3. Results and discussion

3.1. Release process with only sensible heat

The inlet parameters of the particles and the outlet parameters of the

sCO₂ working fluid need to be defined first to design the FB HX. Table 1 presents the target parameters in the design case. For manufacturing issues of the FB HX, the same section for each stage is maintained and change the length of the FB only. The FB HX height of $H_{\text{bed}, i} = 1.0$ m and weight of $W_{\text{bed}, i} = 1.65$ m have been considered. One of the design criteria to lower the cost of the TES is minimizing the length of the heat exchanger tubes. Consequently, the initial focus was on minimizing the tube length required for particles without any chemical reaction. Table S1 shows the optimized length of fluidized bed heat exchanger with inert materials (sensible heat only). The required tube length for the heat exchanger, using limestone as the SH material, is 1193 m, with a fluidized bed volume of 8.03 m³, as shown in Fig. 5(a) (limestone is selected as the sensible heat storage material to facilitate the comparison with the reactive case). The heat loss due to the fluidization gas for one-stage FB HX is 7.49 % as shown in Fig. 5(b). With an increase in the number of stages from 1 to 2, the tube length and fluidized bed volume decrease to 980 m and 6.6 m³, resulting in a reduction of 17.8 % and 18.1 %, respectively. The heat loss due to the fluidization gas decreases to 6.24 %. Further, for the particles in the fluidized bed to mix evenly, the size of each stage is made smaller by increasing the number of stages optimized. When the number of stages is 4, the tube length is reduced to 955 m and the fluidized bed volume is reduced to 6.435 m³. When the number of stages is increased to 6 and 8, the reduction in tube length fluidized bed volume is not significant. Additionally, the performance of the heat exchanger using commercially available CARBO Accucast ID50 particles was assessed [65]. The required tube length for this case is 999 m, with a one-stage fluidized bed volume of 6.732 m³.

As shown in Fig. 6, the required inlet temperature of the sCO₂ gradually decreases as the tube length increases, leading to a reduced outlet temperature of the particles and an increased heat loss of the fluidized gas. The heat loss of the fluidized gas is around 7 % without heat recovery. The heat loss of the fluidization gas is proportional to the mass flow rate of the fluidization gas that depends on the gas velocity and the heat exchanger total horizontal surface area. The tube length change is achieved by changing the length of the heat exchanger maintaining its width and height. The change of the length of the FB HX leads to the increase of the surface area and, consequently, the mass flow rate of the fluidization gas and the associated heat loss. Concerning the effectiveness of heat exchanger, increasing the tube length of the heat exchanger results in increasing the heat exchange area, thus achieving a better heat exchange effect. As defined, the effectiveness indicator does not account for the heat losses in the fluidization gas; it is not an “efficiency”. The heat exchanger achieves a global heat transfer effectiveness over 55 %.

Owing to the strong mixing of fluidized particles, the bed temperature can be considered uniform according to Kunii et al. [54,55], and under this assumption, the direction of flow in the heat exchanger model

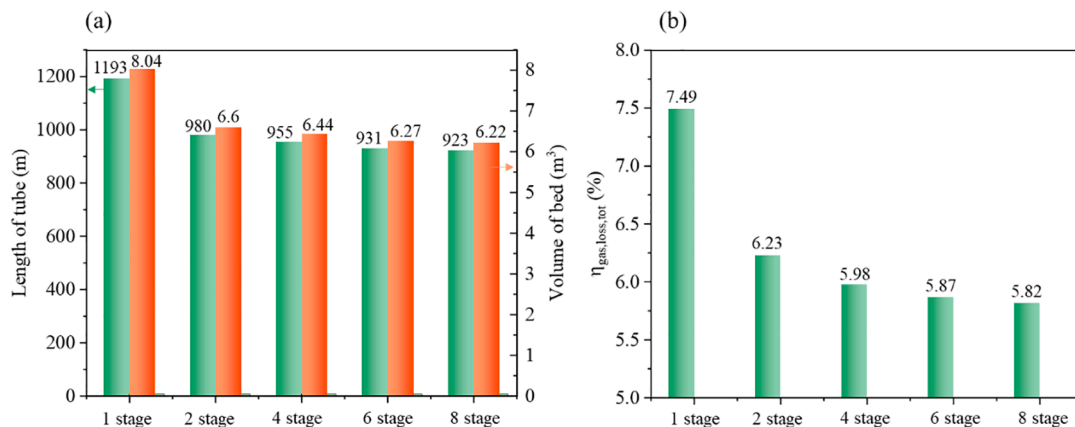


Fig. 5. (a) Required minimum tube length and volume of the fluidized bed and (b) the fluidized gas heat loss for different stages of heat exchangers. ($\bar{u}_{\text{sCO}_2} = \sim 3$ m/s, $m_p = 4.5$ kg/s).

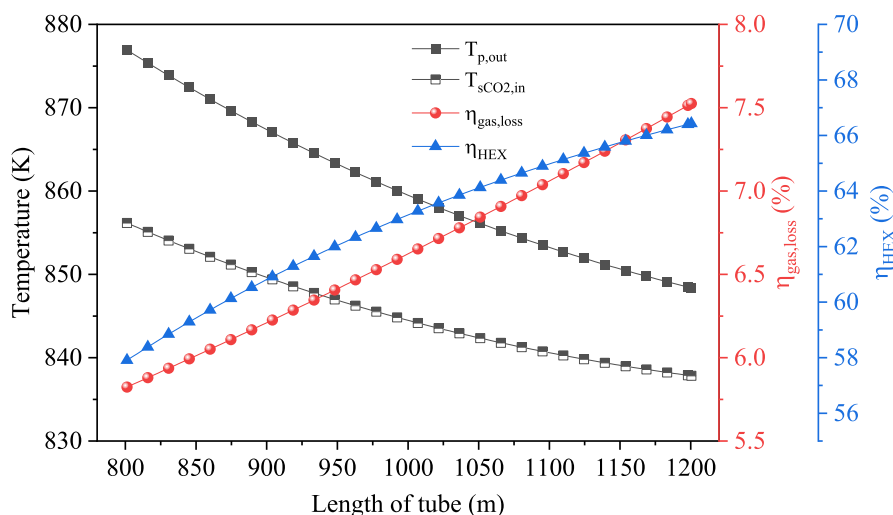


Fig. 6. $s\text{CO}_2$ inlet temperature, particle outlet temperature, and fluidized gas heat loss as a function of the tube length using sensible energy storage materials in one-stage ($\bar{u}_{s\text{CO}_2} = \sim 3 \text{ m/s}$, $m_p = 4.5 \text{ kg/s}$).

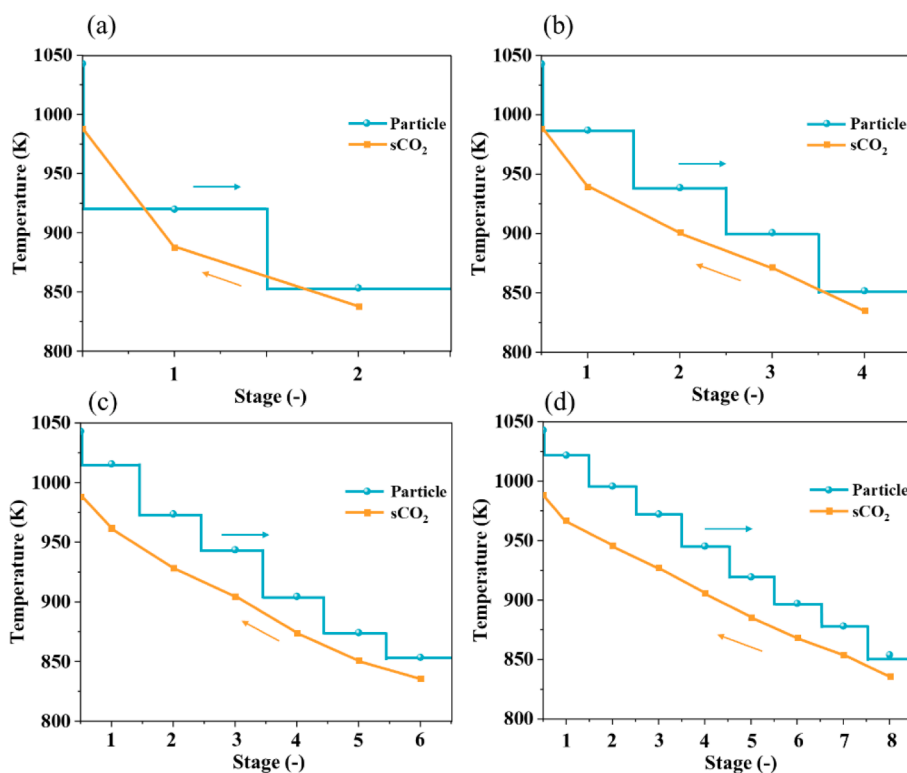


Fig. 7. Inlet and outlet temperatures of the particle and $s\text{CO}_2$ using different stages. (a) two-stages, (b) four-stages, (c) six-stages, and (d) eight-stages.

does not matter. Under this assumption, temperature inversion inside the heat exchanger ($s\text{CO}_2$ temperature larger than particles temperature) can occur. This unexpected phenomenon can be avoided by adding stages. Fig. 7 shows the particle outlet temperature and $s\text{CO}_2$ working medium inlet temperature using different stages. The lines along the way are for visualization purposes only, and they do not necessarily represent the precise temperature evolution inside the FB HX. For the particles, the horizontal line represents the uniform temperature of the FB HX, which is caused by the high mixing rate of the particles, and the vertical line represents an almost instantaneous drop in the particle temperature at the entrance of each stage, which is due to the heat balance method used in the modeling. Fig. 7(a) is not realistic because in some location the $T_{s\text{CO}_2,\text{in}}$ is higher than the $T_{p,\text{out}}$. Therefore, this

configuration is unacceptable.

3.2. Release process with chemical reaction

By optimizing the particle mass flow rate and heat exchanger design for a one-stage reactor utilizing a reactive material, the result shows that a particle mass flow rate of 0.39 kg/s is required for the one-stage reactor. Table S2 shows the optimized size of fluidized bed heat exchanger with chemical reaction. The particle mass flow rate needed in the one-stage carbonator is 11.5 times lower than that of the sensible thermal storage materials. A lower particle mass flow rate can significantly reduce the costs associated with storage tanks and particle materials in thermal storage systems. Fig. 8(a) shows that reducing the

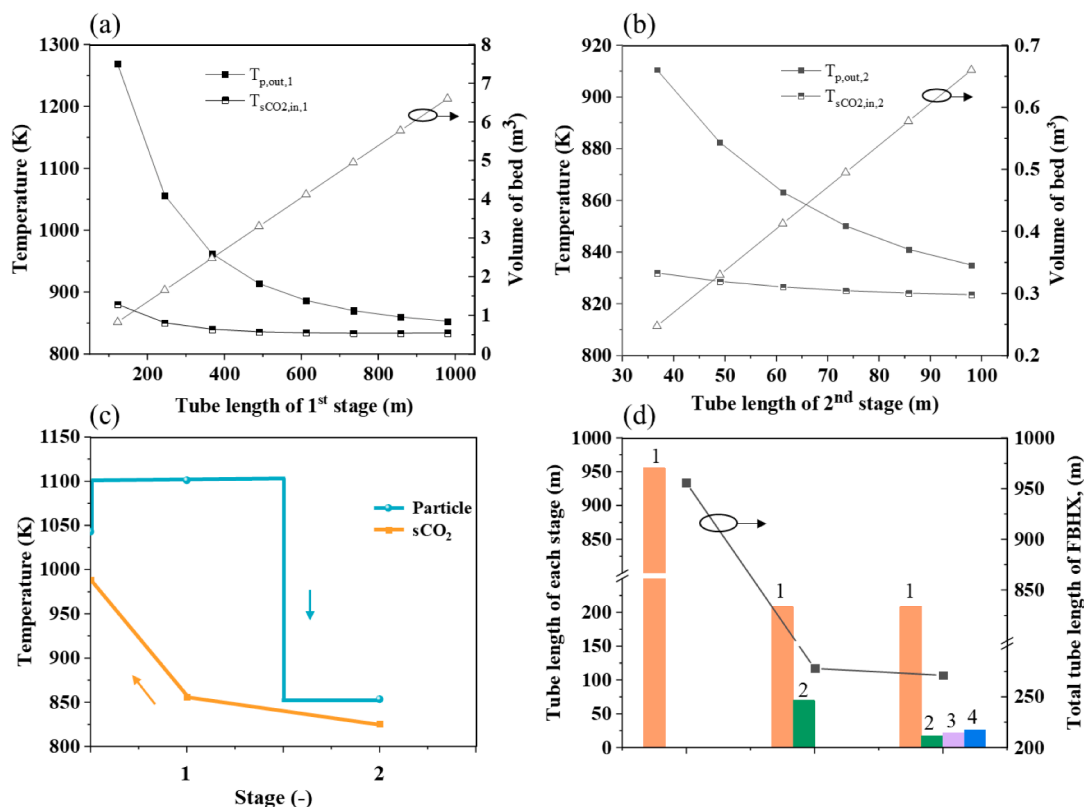


Fig. 8. Required minimum tube length for the heat exchanger using different stages ($\bar{u}_{sCO_2} = \sim 3$ m/s, $m_p = 0.39$ kg/s). Stage numbers are indicated as 1 to 4, with 1 being the particle inlet stage.

lengths of the heat exchanger tubes leads to a gradual increase in the particle outlet temperature. To maximize sensible heat utilization, the tube length is increased to 955 m, which reduces the particle temperature to a target value of 853 K. Compared to sensible thermal storage, the improvement in tube length is not significant. However, the lengths of the heat exchanger tubes can be further optimized by increasing the number of fluidized bed stages.

In a two-stage reactive heat exchanger, the first stage primarily transfers the heat released by the chemical reaction to sCO_2 , while the second stage utilizes the sensible heat of the particles to heat the working fluid. As shown in Fig. 8(a), the particle outlet temperature of the first stage increases as the tube length decreases. However, a high particle temperature can damage heat exchanger tubes. Therefore, the first-stage heat exchanger is limited by the constraint in which the maximum particle temperature within the heat exchanger should not

exceed 1100 K due to material limitations. For a limestone thermal storage material with a particle mass flow rate of 0.39 kg/s, the dimensions of the first stage are $1.65 \times 0.85 \times 1.0$ m³, with a tube length of 208 m, satisfying the requirement of the first-stage particle outlet temperature of 1100 K. The second-stage, which utilizes the large temperature difference between the inlet and outlet particles to heat the working fluid with a small temperature difference, requires much smaller dimensions of $1.65 \times 0.285 \times 1.0$ m³ and a tube length of 69.8 m, as shown in Fig. 8(b). Using a two-stage heat exchanger, the outlet temperature of the particles can be lower than 853 K, and the sCO_2 working temperature is lower than 838 K as shown in Fig. 8(c). Furthermore, an evaluation of a four-stage HX was conducted. Fig. 8(d) shows a comparison of the tube lengths of heat exchangers with three different numbers of stages. The results indicate that the four-stage heat exchanger requires a tube length of 271 m, highlighting a limited

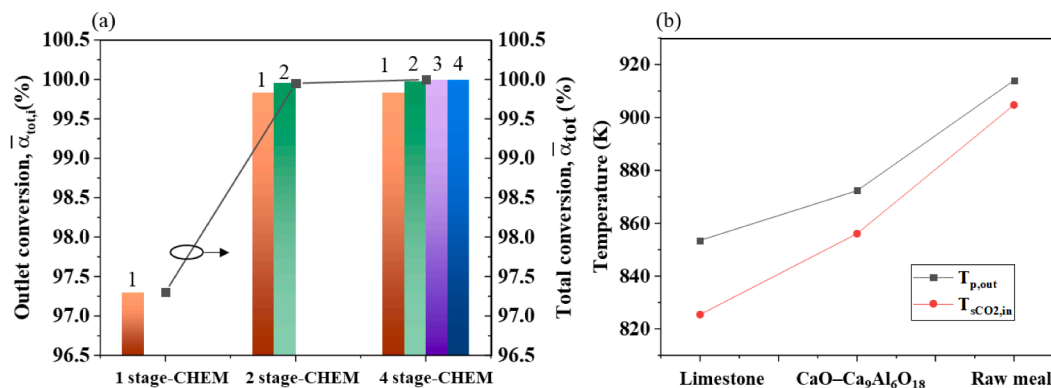


Fig. 9. (a) Conversion of limestone in the heat exchanger for different stages. (b) Outlet particle temperatures and inlet sCO_2 temperatures of two stages using three Ca-based materials.

opportunity for further optimization. This limitation arises from the necessity to restrict the particle outlet temperature of the first stage below 1100 K. However, as depicted in Fig. 8 (a), there is potential for further reductions in the length of reactive heat exchangers if the temperature tolerance on the materials used can be enhanced. Therefore, the two-stage heat exchanger offers a great opportunity for heat exchange processes involving gas–solid chemical reactions.

For a one-stage heat exchanger, the average conversion is 97.3 %, which is lower than the 99.95 % achieved by the two-stage heat exchanger (Fig. 9(a)). This difference can be attributed to the large residence time of the reactive particles in the two-stage HX. A similar pattern is observed for the four-stage heat exchanger. The overall conversion at the outlet of the FB HX follows the order of four-stage > two-stage > one-stage. As illustrated in Fig. 9(b), different CaCO₃-based materials exhibit significant variations in the inlet temperature of the sCO₂ working fluid and the outlet temperature of the particles for the two-stage heat exchanger due to differences in the CaO mass fraction. The higher the mass fraction of in material is (the more energy is released) resulting in a lower inlet temperature of the sCO₂ working fluid.

The cost is related to a FB HX system with a 1-MW_t heat duty. The heat exchanger specific cost estimate includes heat transfer tube material cost and heat storage material cost. The optimized particle mass flow and heat exchanger length using inert material (sensible heat, SH) are 4.5 kg/s and 1193 m. The optimized particle mass flow and heat exchanger tube length using reactive material (sensible and chemical heat, SCH) are 0.39 kg/s and 278 m. Based on previous values, the costs of the heat exchanger based on SH and SCH storage materials are \$925.48/kW_t and \$228.78/kW_t, respectively. The sensible heat FB HX costs 4 times more than the SCH heat exchanger. The volume of the former is $V_{FBHX} = V_{FBHX,1} + V_{FBHX,2} = 1.815 + 4.785 = 6.6m^3$. The volume of the later is $V_{FBHX} = V_{FBHX,1} + V_{FBHX,2} = 1.4025 + 0.47025 = 1.87275m^3$. Consequently, the power densities are 151.5 kW/m³ and 534 kW/m³ for SH and CSH heat exchangers, respectively.

3.3. Sensitivity analysis

It is highly essential to investigate the influences of key parameters on the performance of particle-sCO₂ heat exchangers. The influences of

the particle inlet temperature, sCO₂ mass flow rate, tube diameter, and particle specific surface area on the design characteristics of the two-stage reactive heat exchanger are illustrated in Fig. 10. The geometric parameters of the FB HX are based on two-stages in Table. S2.

Fig. 10(a) presents a plot of the variations in particle outlet temperature, working fluid inlet temperature, heat exchanger efficiency, and overall conversion of the outlet particles as a function of the particle inlet temperature. When the particle inlet temperature decreases from 1095 K to 995 K, the required sCO₂ working fluid inlet temperature increases from 819.7 K to 836.6 K, resulting in a mere 0.17 % change in the overall conversion of the particles. This small change can be attributed to the reduced heat transported by the working fluid due to the decrease in particle temperature, increasing the inlet temperature of the working fluid. The variation in particle inlet temperature contributes to a remarkable increase in heat exchanger efficiency from 52.7 % to 67.2 %.

The increase in the sCO₂ mass flow rate (Fig. 10(b)) increases the heat transfer rate transported by the working fluid. Considering the constant particle mass flow rate, maintaining the system heat duty requires a relatively high inlet temperature for the working fluid. In turn, the increase in the working fluid temperature causes an increase in the particle outlet temperature. However, these small temperature variations have negligible effects on the heat exchanger efficiency and the overall conversion, with changes of merely 1.3 % and 0.004 %, respectively.

The diameter of the tubes affects the arrangement. An increase in the tube diameter (Fig. 10(c)) results in an increase in the horizontal gap between tube centers, vertical gap between tube centers, and minimum horizontal gap between container walls and closer tubes, thereby reducing the lengths of the heat exchanger tubes. With a sufficient tube length, the heat released by the chemical reaction is mainly transferred to the working fluid in the first stage, while the second stage valorizes the sensible heat of the particles. However, if the tube length is insufficient, the sensible heat cannot be transported, leading to an increase in the particle outlet temperature and an increase in the particle conversion. Furthermore, the overall heat transfer coefficient of the heat exchanger decreases with increasing tube diameter. The interaction of these two factors results in a decrease in the overall efficiency of the HX.

The microstructural parameters of particles can influence

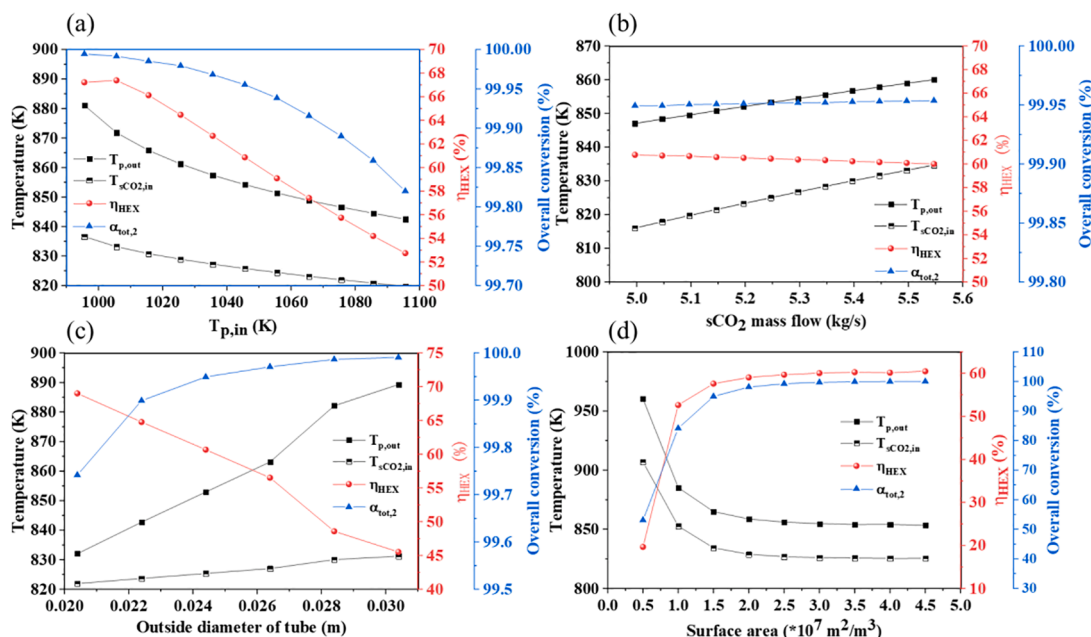


Fig. 10. Particle outlet temperature, sCO₂ inlet temperature, overall efficiency, and overall outlet conversion of the FB HX varying with (a) particle inlet temperature, (b) sCO₂ mass flow, (c) outside diameter of tube, and (d) particle surface area.

intraparticle diffusion and consequently affect the conversion. CaL materials often experience a decay in activity due to high-temperature sintering during the cyclic process. To investigate the variations in particle conversion during multiple cycles of heat storage and release, the influence of the surface area (S_0) on the conversion was evaluated (Fig. 10(d)). For a specific surface area of $5 \times 10^6 \text{ m}^2/\text{m}^3$, the overall particle conversion at the outlet of the heat exchanger reaches 53.08 %, resulting in an increased required sCO₂ inlet temperature and elevated particle outlet temperature. The efficiency of the heat exchanger is only 19.6 % under this condition. With an increase in S_0 , the overall conversion increases, the required sCO₂ inlet temperature gradually decreases, and the efficiency of the heat exchanger improves. The overall particle conversion exceeds 98 % for specific surface areas larger than $2 \cdot 10^7 \text{ m}^2/\text{m}^3$.

4. Conclusions

The design and optimization of fluidized bed heat exchangers with sensible and chemical heat release characteristics was carried out. The objective of the work was to design a multistage heat exchanger to provide heat to an sCO₂ cycle integrated into a CSP plant operating at sCO₂ inlet temperatures $\geq 988 \text{ K}$, sCO₂ pressures reaching 20 MPa, and particle temperatures of $\sim 1048 \text{ K}$ and to compare sensible and thermochemical technologies. The reference thermal duty of the heat exchanger is 1-MW_t. The findings provide valuable insights into the performance and efficiency of the heat exchanger under different conditions. The main results can be summarized as follows:

1. For the sensible heat release process, the results reveal that the minimum total tube length required is 1193 m. With an increase from one to two stages, the tube length can be reduced to 980 m (17.8 % reduction). For the chemical heat release process, the particle mass flow rate reduction is 11.5 times that of the sensible-only thermal storage HX.
2. The length of the heat exchanger tubes is reduced by increasing the number of stages, and the two-stage heat exchanger shows promising results for applications involving gas–solid chemical reactions. The carbonator total tube length is 278 m, which is 3.5 times shorter than for the two-stage sensible HX. This gain has a high impact on the cost of the heat exchanger since it is roughly proportional to the total tube length.
3. In the two-stage heat exchanger, the carbonation reaction reaches near completion in the first high-temperature stage, whereas particle sensible heat is released in the second stage.
4. Sensitivity analysis indicates that the variations in particle inlet temperature and sCO₂ mass flow rate have negligible effects on the heat exchanger efficiency and overall conversion. However, increasing the tube diameter leads to both a decrease in heat transfer coefficients and a significant increase in global heat transfer efficiency. The particle surface area significantly affects the reaction conversion inside the heat exchanger. The model can also be used to predict the performance and design parameters of the heat exchanger using Ca-based materials after multiple cycles.

Overall, the findings contribute to the development of highly efficient, compact, and cost-effective thermochemical storage systems.

CRedit authorship contribution statement

Hangbin Zheng: Writing – original draft, Software, Formal analysis, Conceptualization. **Xianglei Liu:** Writing – review & editing, Funding acquisition, Data curation. **Gilles Flamant:** Writing – review & editing, Supervision, Methodology, Funding acquisition, Data curation, Conceptualization.

Declaration of competing interest

The authors declare that they have no known competing financial interests or personal relationships that could have appeared to influence the work reported in this paper.

Data availability

Data will be made available on request.

Acknowledgments

This work was supported by the National Natural Science Foundation of China (No. 51820105010) and the French Investments for the Future program managed by the National Agency for Research (ANR) under contract ANR-10-LABX-22-01. HB wants to give thanks for the support from the Postgraduate Research & Practice Innovation Program of Jiangsu Province (No. KYCX21_0210) and the China Scholarship Council (202106830083).

Appendix A. Supplementary data

Supplementary data to this article can be found online at <https://doi.org/10.1016/j.cej.2024.151305>.

References

- [1] N.S. Lewis, D.G. Nocera, Powering the planet: Chemical challenges in solar energy utilization, *Proc. Natl. Acad. Sci.* 103 (2006) 15729–15735.
- [2] A.J. Carrillo, J. González-Aguilar, M. Romero, J.M. Coronado, Solar energy on demand: a review on high temperature thermochemical heat storage systems and materials, *Chem. Rev.* 119 (2019) 4777–4816.
- [3] S. Wang, K. Luo, J. Fan, CFD-DEM coupled with thermochemical sub-models for biomass gasification: Validation and sensitivity analysis, *Chem. Eng. Sci.* 217 (2020) 115550.
- [4] S. Wang, K. Luo, C. Hu, J. Lin, J. Fan, CFD-DEM simulation of heat transfer in fluidized beds: Model verification, validation, and application, *Chem. Eng. Sci.* 197 (2019) 280–295.
- [5] H. Liang, R. Su, W. Huang, Z. Cheng, F. Wang, G. Huang, et al., A novel spectral beam splitting photovoltaic/thermal hybrid system based on semi-transparent solar cell with serrated groove structure for co-generation of electricity and high-grade thermal energy, *Eng. Convers. Manage.* 252 (2022) 115049.
- [6] L. Zheng, Y. Xuan, J. Wang, S. Bao, X. Liu, K. Zhang, Inverted perovskite/silicon V-shaped tandem solar cells with 27.6% efficiency via self-assembled monolayer-modified nickel oxide layer, *J. Mater. Chem. A* 10 (2022) 7251–7262.
- [7] G. Flamant, B. Grange, J. Wheeldon, F. Siros, B. Valentin, F. Bataille, et al., Opportunities and challenges in using particle circulation loops for concentrated solar power applications, *Prog. Energy Combust. Sci.* 94 (2023) 101056.
- [8] A. Touzo, Q. Falcoz, G. Flamant, Thermal Energy Storage, Fundamentals and Applications, Concentrating Solar Thermal Energy, 2022, pp. 229–258.
- [9] C. Ortiz, J.M. Valverde, R. Chacartegui, L.A. Perez-Maqueada, P. Giménez, The Calcium-Looping (CaCO₃/CaO) process for thermochemical energy storage in Concentrating Solar Power plants, *Renew. Sustain. Energy Rev.* 113 (2019) 109252.
- [10] L. André, S. Abanades, G. Flamant, Screening of thermochemical systems based on solid-gas reversible reactions for high temperature solar thermal energy storage, *Renew. Sustain. Energy Rev.* 64 (2016) 703–715.
- [11] M. Romero, A. Steinfeld, Concentrating solar thermal power and thermochemical fuels, *Eng. Environ. Sci.* 5 (2012) 9234–9245.
- [12] Feldman D, Margolis R, Denholm P, Stekli J. Exploring the potential competitiveness of utility-scale photovoltaics plus batteries with concentrating solar power, 2015–2030. United States 2016.
- [13] H. Zhang, J. Baeyens, G. Cáceres, J. Degève, Y. Lv, Thermal energy storage: Recent developments and practical aspects, *Prog. Energy Combust. Sci.* 53 (2016) 1–40.
- [14] C. Zhao, J. Yan, X. Tian, X. Xue, Y. Zhao, Progress in thermal energy storage technologies for achieving carbon neutrality, *Carbon Neutrality.* 2 (2023).
- [15] M. Yang, M.A. Moghimi, R. Loillier, C.N. Markides, M. Kadivar, Design of a latent heat thermal energy storage system under simultaneous charging and discharging for solar domestic hot water applications, *Appl. Energy* 336 (2023).
- [16] Z. Ge, B. Dou, L. Wang, Y. Ding, H. Chen, Y. Xuan, Calcium-looping based energy conversion and storage for carbon neutrality – the way forward, *Carbon Neutrality.* 1 (2022).
- [17] S. Ströhle, A. Haselbacher, Z.R. Jovanovic, A. Steinfeld, The effect of the gas–solid contacting pattern in a high-temperature thermochemical energy storage on the performance of a concentrated solar power plant, *Eng. Environ. Sci.* 9 (2016) 1375–1389.

- [18] G. Colelli, R. Chacartegui, C. Ortiz, A. Carro, A.P. Arena, V. Verda, Life cycle and environmental assessment of calcium looping (CaL) in solar thermochemical energy storage, *Energ. Convers. Manage.* 257 (2022) 115428.
- [19] H. Zheng, C. Song, C. Bao, X. Liu, Y. Xuan, Y. Li, et al., Dark calcium carbonate particles for simultaneous full-spectrum solar thermal conversion and large-capacity thermochemical energy storage, *Sol. Energy Mater. Sol. Cells* 207 (2020) 110364.
- [20] H. Zheng, X. Liu, Y. Xuan, C. Song, D. Liu, Q. Zhu, et al., Thermochemical heat storage performances of fluidized black CaCO₃ pellets under direct concentrated solar irradiation, *Renew. Energy* 178 (2021) 1353–1369.
- [21] A. Alovio, R. Chacartegui, C. Ortiz, J.M. Valverde, V. Verda, Optimizing the CSP-Calcium Looping integration for Thermochemical Energy Storage, *Energ. Convers. Manage.* 136 (2017) 85–98.
- [22] R. Chacartegui, A. Alovio, C. Ortiz, J.M. Valverde, V. Verda, J.A. Becerra, Thermochemical energy storage of concentrated solar power by integration of the calcium looping process and a CO₂ power cycle, *Appl. Energy* 173 (2016) 589–605.
- [23] M.A. Naeem, A. Armutlulu, Q. Intiaz, F. Donat, R. Schäublin, A. Kierzkowska, et al., Optimization of the structural characteristics of CaO and its effective stabilization yield high-capacity CO₂ sorbents, *Nat. Commun.* 9 (2018) 2408.
- [24] Y. Yang, Y. Li, X. Yan, J. Zhao, C. Zhang, Development of thermochemical heat storage based on CaO/CaCO₃ cycles: A review, *Energies* (2021).
- [25] M. Benitez-Guerrero, J.M. Valverde, P.E. Sanchez-Jimenez, A. Perejon, L.A. Perez-Maqueda, Multicycle activity of natural CaCO₃ minerals for thermochemical energy storage in Concentrated Solar Power plants, *Sol. Energy* 153 (2017) 188–199.
- [26] C. Tregambi, S. Padula, M. Galbusieri, G. Coppola, F. Montagnaro, P. Salatino, et al., Directly irradiated fluidized bed reactor for thermochemical energy storage and solar fuels production, *Powder Technol.* 366 (2020) 460–469.
- [27] T. Esence, H. Benoit, D. Poncin, M. Tessonneau, G. Flamant, A shallow cross-flow fluidized-bed solar reactor for continuous calcination processes, *Sol. Energy* 196 (2020) 389–398.
- [28] H. Zheng, X. Liu, Y. Xuan, Y. Ding, G. Flamant, Efficient direct solar-driven thermochemical energy storage of (AlMgFeMn)OxCaCO₃ pellets in a fluidized bed reactor, *Energ. Convers. Manage.* 285 (2023).
- [29] T. Esence, E. Guillot, M. Tessonneau, J.-L. Sans, G. Flamant, Solar calcination at pilot scale in a continuous flow multistage horizontal fluidized bed, *Sol. Energy* 207 (2020) 367–378.
- [30] G. Flamant, D. Hernandez, C. Bonet, J.-P. Traverse, Experimental aspects of the thermochemical conversion of solar energy; Decarbonation of CaCO₃, *Sol. Energy* 24 (1980) 385–395.
- [31] C. Tregambi, F. Di Lauro, S. Pascual, P. Lisbona, L.M. Romeo, R. Solimene, et al., Solar-driven calcium looping in fluidized beds for thermochemical energy storage, *Chem. Eng. J.* 466 (2023) 142708.
- [32] P. Pasabeyoglu, G. Moumin, L. de Oliveira, M. Roeb, B. Akata, Solarization of the zeolite production: Calcination of kaolin as proof-of-concept, *J. Clean. Prod.* 414 (2023) 137611.
- [33] M. Ebert, L. Amsbeck, J. Rheinländer, B. Schlögl-Knothe, S. Schmitz, M. Sibum, et al., Operational experience of a centrifugal particle receiver prototype, *AIP Conference Proceedings* 2126 (2019).
- [34] Z. Ma, J. Martinek, Analysis of a fluidized-bed particle/supercritical-CO₂ heat exchanger in a concentrating solar power system, *J. Sol. Energy Eng.* 143 (2020).
- [35] C.K. Ho, High-temperature particle heat exchanger for sCO₂ power cycles (2020 SETO poster), United States (2020).
- [36] R. Chen, M. Romero, J. González-Aguilar, F. Rovense, Z. Rao, S. Liao, Design and off-design performance comparison of supercritical carbon dioxide Brayton cycles for particle-based high temperature concentrating solar power plants, *Energ. Convers. Manage.* 232 (2021) 113870.
- [37] K. Wang, M.-J. Li, J.-Q. Guo, P. Li, Z.-B. Liu, A systematic comparison of different S-CO₂ Brayton cycle layouts based on multi-objective optimization for applications in solar power tower plants, *Appl. Energy* 212 (2018) 109–121.
- [38] L. Fedunik-Hofman, A. Bayon, S.W. Donne, Kinetics of solid-gas reactions and their application to carbonate looping systems, *Energies* (2019).
- [39] Z. Zhou, P. Xu, M. Xie, Z. Cheng, W. Yuan, Modeling of the carbonation kinetics of a synthetic CaO-based sorbent, *Chem. Eng. Sci.* 95 (2013) 283–290.
- [40] J.M. López, G. Grasa, R. Murillo, Evaluation of the effect of inert support on the carbonation reaction of synthetic CaO-based CO₂ sorbents, *Chem. Eng. J.* 350 (2018) 559–572.
- [41] Z. Li, General rate equation theory for gas–solid reaction kinetics and its application to CaO carbonation, *Chemical Engineering Sci.* 227 (2020) 115902.
- [42] K.J. Albrecht, M.D. Carlson, H.F. Laubscher, R. Crandell, N. DeLovato, C.K. Ho, Testing and model validation of a prototype moving packed-bed particle-to-sCO₂ heat exchanger, *AIP Conference Proceedings* 2303 (2020) 030002.
- [43] Weast T, Shannon LJ. *Thermal energy storage systems using fluidized bed heat exchangers*. 1980.
- [44] I.H. Farag, S.B. Reddy Karri, R. Breault, K.Y. Tsai, Graphical solution of multistage fluidized bed heat exchanger, *Chem. Eng. Commun.* 48 (1986) 331–348.
- [45] F. Gomez-Garcia, D. Gauthier, G. Flamant, Design and performance of a multistage fluidised bed heat exchanger for particle-receiver solar power plants with storage, *Appl. Energy* 190 (2017) 510–523.
- [46] Z. Ma, J. Gifford, X. Wang, J. Martinek, Electric-thermal energy storage using solid particles as storage media, *Joule*. 7 (2023) 843–848.
- [47] T. Baumann, S. Zunft, Development and Performance Assessment of a Moving Bed Heat Exchanger for Solar Central Receiver Power Plants, *Energy Procedia* 69 (2015) 748–757.
- [48] B.D. Iverson, T.M. Conboy, J.J. Pasch, A.M. Kruizenga, Supercritical CO₂ Brayton cycles for solar-thermal energy, *Appl. Energy* 111 (2013) 957–970.
- [49] T. Neises, C. Turchi, A Comparison of Supercritical Carbon Dioxide Power Cycle Configurations with an Emphasis on CSP Applications, *Energy Procedia* 49 (2014) 1187–1196.
- [50] Colebrook CF, White CM, Taylor GI. Experiments with fluid friction in roughened pipes. *Proceedings of the Royal Society of London Series A - Mathematical and Physical Sciences*. 1997;161:367-81.
- [51] V. Gniewinski, On heat transfer in tubes, *Int. J. Heat Mass Transf.* 63 (2013) 134–140.
- [52] Lemmon EW, Huber ML, McLinden MO. NIST Standard reference database 23: Reference fluid thermodynamic and transport properties-REFPROP, Version 9.1 | NIST. 2013.
- [53] V. Thonglimp, N. Hiquily, C. Laguerie, Vitesse minimale de fluidisation et expansion des couches de mélanges de particules solides fluidisées par un gaz, *Powder Technol.* 38 (1984) 233–253.
- [54] D. Kunii, O. Levenspiel, CHAPTER 8 - High-Velocity Fluidization, in: D. Kunii, O. Levenspiel (Eds.), *Fluidization Engineering*, Second Edition, Butterworth-Heinemann, Boston, 1991, pp. 193–210.
- [55] D. Kunii, O. Levenspiel, CHAPTER 9 - Solid Movement: Mixing, Segregation, and Staging, in: D. Kunii, O. Levenspiel (Eds.), *Fluidization Engineering*, Second Edition, Butterworth-Heinemann, Boston, 1991, pp. 211–235.
- [56] N.S. Grewal, S.C. Saxena, Heat transfer between a horizontal tube and a gas-solid fluidized bed, *Int. J. Heat Mass Transf.* 23 (1980) 1505–1519.
- [57] V. Stenberg, V. Sköldberg, L. Öhrby, M. Rydén, Evaluation of bed-to-tube surface heat transfer coefficient for a horizontal tube in bubbling fluidized bed at high temperature, *Powder Technol.* 352 (2019) 488–500.
- [58] S. Lechner, M. Merzsch, H.J. Krautz, Heat-transfer from horizontal tube bundles into fluidized beds with Geldart A lignite particles, *Powder Technol.* 253 (2014) 14–21.
- [59] N. Hu, A.W. Scaroni, Calcination of pulverized limestone particles under furnace injection conditions, *Fuel* 75 (1996) 177–186.
- [60] Y.A. Criado, B. Arias, J.C. Abanades, Effect of the carbonation temperature on the CO₂ carrying capacity of CaO, *Ind. Eng. Chem. Res.* 57 (2018) 12595–12599.
- [61] J. Plou, I. Martínez, G. Grasa, R. Murillo, Reactivity of calcined cement raw meals for carbonation, *Powder Technol.* 354 (2019) 338–347.
- [62] J.B. Rawlings, J.G. Ekerdt, *Chemical reactor analysis and design fundamentals*, Nob Hill Pub, Llc (2002).
- [63] Buck R. G3P3 Techno-Economic Analysis of UpScaled CentRec® Receiver. 2021, Available from: <<https://elib.dlr.de/140177/>>.
- [64] R. Buck, J. Sment, Techno-economic analysis of multi-tower solar particle power plants, *Sol. Energy* 254 (2023) 112–122.
- [65] C.K. Ho, J.M. Christian, D. Romano, J. Yellowhair, N. Siegel, L. Savoldi, et al., Characterization of particle flow in a free-falling solar particle receiver, *J. Sol. Energy Eng.* 139 (2016).